Monthly Notices
of the
ROYAL ASTRONOMICAL SOCIETY

Mon. Not. R. Astron. Soc. **424,** 1042–1060 (2012) doi:10.1111/j.1365-2966.2012.21278.x

Residual cooling and persistent star formation amid active galactic nucleus feedback in Abell 2597

G. R. Tremblay,[1,2,3⋆] C. P. O'Dea,[2,4] S. A. Baum,[3,5] T. E. Clarke,[6] C. L. Sarazin,[7] J. N. Bregman,[8] F. Combes,[9] M. Donahue,[10] A. C. Edge,[11] A. C. Fabian,[12] G. J. Ferland,[13] B. R. McNamara,[4,14] R. Mittal,[3] J. B. R. Oonk,[15] A. C. Quillen,[16] H. R. Russell,[14] J. S. Sanders,[12] P. Salomé,[9] G. M. Voit,[10] R. J. Wilman[11] and M. W. Wise[15]

[1]*European Southern Observatory, Karl-Schwarzschild-Str. 2, 85748 Garching bei München, Germany*
[2]*Department of Physics, Rochester Institute of Technology, 84 Lomb Memorial Drive, Rochester, NY 14623, USA*
[3]*Chester F. Carlson Center for Imaging Science, 54 Lomb Memorial Drive, Rochester, NY 14623, USA*
[4]*Harvard–Smithsonian Center for Astrophysics, 60 Garden Street, Cambridge, MA 02138, USA*
[5]*Radcliffe Institute for Advanced Study, 10 Garden Street, Cambridge, MA 02138, USA*
[6]*Naval Research Laboratory Remote Sensing Division, Code 7213 4555 Overlook Avenue SW, Washington, DC 20375, USA*
[7]*Department of Astronomy, University of Virginia, PO Box 400325, Charlottesville, VA 22904-4325, USA*
[8]*Department of Astronomy, University of Michigan, Ann Arbor, MI 48109, USA*
[9]*Observatoire de Paris, LERMA, CNRS, 61 Av. de l'Observatoire, 75014 Paris, France*
[10]*Physics and Astronomy Department, Michigan State University, East Lansing, MI 48824-2320, USA*
[11]*Department of Physics, Durham University, Durham DH1 3LE*
[12]*Institute of Astronomy, Madingley Road, Cambridge CB3 0HA*
[13]*Department of Physics, University of Kentucky, Lexington, KY 40506, USA*
[14]*Physics and Astronomy Department, Waterloo University, 200 University Avenue W., Waterloo, ON N2L 2G1, Canada*
[15]*ASTRON, Netherlands Institute for Radio Astronomy, PO Box 2, 7990 AA Dwingeloo, the Netherlands*
[16]*Department of Physics and Astronomy, University of Rochester, Rochester, NY 14627, USA*

Accepted 2012 May 9. Received 2012 May 8; in original form 2012 March 1

ABSTRACT

New *Chandra* X-ray and *Herschel* Far-Infrared (FIR) observations enable a multiwavelength study of active galactic nucleus (AGN) heating and intracluster medium (ICM) cooling in the brightest cluster galaxy (BCG) of Abell 2597 ($z = 0.0821$). The new *Chandra* observations reveal the central $\lesssim$30 kpc X-ray cavity network to be more extensive than previously thought, and associated with enough enthalpy to theoretically inhibit the inferred classical cooling flow. Nevertheless, we present new evidence, consistent with previous results, that a moderately strong residual cooling flow is persisting at 4–8 per cent of the classically predicted rates in a spatially structured manner amid the feedback-driven excavation of the X-ray cavity network. New *Herschel* observations are used to estimate warm and cold dust masses, a lower limit gas-to-dust ratio and a star formation rate consistent with previous measurements. [O I] and CO(2−1) line profiles are used to constrain the kinematics of the $\sim 10^9$ $M_\odot$ reservoir of cold molecular gas. The cooling time profile of the ambient X-ray atmosphere is used to map the locations of the observational star formation entropy threshold as well as the theoretical thermal instability threshold. Both lie just outside the $\lesssim$30-kpc central region permeated by X-ray cavities, and star formation as well as ionized and molecular gas lie interior to both. The young stars are distributed in an elongated region that is aligned with the radio lobes, and their estimated ages are both younger and older than the X-ray cavity network, suggesting both jet-triggered as well as persistent star formation over the current AGN feedback episode. Bright

⋆E-mail: grant.tremblay@eso.org

X-ray knots that are coincident with extended Lyα and far-ultraviolet continuum filaments motivate a discussion of structured cooling from the ambient hot atmosphere along a projected axis that is perpendicular to X-ray cavity and radio axis. We conclude that the cooling ICM is the dominant contributor of the cold gas reservoir fuelling star formation and AGN activity in the Abell 2597 BCG.

Key words: galaxies: active – galaxies: clusters: general – galaxies: clusters: individual: Abell 2597 – galaxies: clusters: intracluster medium – galaxies: star formation.

1 INTRODUCTION

For a subset of galaxy clusters with sharply peaked X-ray surface brightness profiles, the intracluster medium (ICM; e.g. Sarazin 1986) can cool via bremsstrahlung processes from $>10^7$ to $\ll 10^4$ K on time-scales much shorter than a Gyr within a radius of $\sim$100 kpc. Simple models predict that runaway entropy loss by gas within this radius accompanies subsonic, nearly isobaric compression by the ambient hot reservoir, driving a long-lived classical cooling flow on to the central brightest cluster galaxy (hereafter BCG; see cooling flow reviews by Fabian 1994; Peterson & Fabian 2006). In these 'cool core' (CC) clusters, catastrophic condensation of the ICM should drive extreme star formation rates (10^2–10^3 $M_\odot$ yr^{-1}) amid massive cold gas reservoirs ($\sim 10^{12}$ $M_\odot$) in the BCG, and high-resolution X-ray spectroscopy should detect bright coolant lines stemming from $\lesssim 10^3$ $M_\odot$ cascades of multiphase gas condensing from the hot atmosphere. Yet three decades of searches for these expected cooling flow mass sinks returned with results that were orders of magnitude below predictions, consistent only with residual cooling at $\sim$1–10 per cent of the expected rates (e.g. Allen 1969, 1995; De Young & Roberts 1974; Baan, Haschick & Burke 1978; Haynes, Brown & Roberts 1978; Peterson 1978; Shostak et al. 1980; O'Dea & Baum 1987, 1997; McNamara & O'Connell 1989; O'Dea et al. 1994a; O'Dea, Payne & Kocevski 1998; Peres et al. 1998; Mittaz et al. 2001; Peterson et al. 2001, 2003; Tamura et al. 2001; Sakelliou et al. 2002; Xu et al. 2002; Edge & Frayer 2003; Bregman & Lloyd-Davies 2006; Sanders et al. 2008).

Attempts to reconcile these results with the high X-ray luminosities and long lifetimes associated with the CC phase have invoked non-gravitational heating mechanisms to inhibit or replenish an average $\sim$90 per cent of ICM radiative losses over the cluster lifetime (e.g. review by Peterson & Fabian 2006). One promising candidate for quenching cooling flows in the innermost regions of cool cores is a feedback loop regulated by the mechanical dissipation of active galactic nucleus (AGN) power (e.g. Rosner & Tucker 1989; Baum & O'Dea 1991; Churazov et al. 2002; Bîrzan et al. 2004; Dunn & Fabian 2006; Rafferty et al. 2006; Best et al. 2007; Edwards et al. 2007; Mittal et al. 2009, reviews by McNamara & Nulsen 2007, 2012; Fabian 2012). The paradigm is supported by strong circumstantial evidence, including observations of kiloparsec (kpc) scale X-ray cavities in spatial correlation with radio emission associated with AGN outflows (Böhringer et al. 1993; Fabian et al. 2000, 2006; McNamara et al. 2000, 2001; Blanton et al. 2001; Churazov et al. 2001; Bîrzan et al. 2004; Forman et al. 2005, 2007; Nulsen et al. 2005). The power of these radio sources are statistically correlated with X-ray luminosity from within the cooling radius, and the most radio-loud BCGs are ubiquitously associated with the strongest cool cores (e.g. Burns 1990; Bîrzan et al. 2004; Rafferty et al. 2006; Mittal et al. 2009; Sun 2009; Hudson et al. 2010).

Observationally supported simulations show that the outflowing plasma can drive sound waves and subsonically excavate cavities in the thermal gas, which then buoyantly rise, entrain magnetic fields and colder interstellar medium (ISM) phases, and locally thermalize enthalpy associated with their inflation as ambient gas moves to refill their wakes (e.g. Begelman 2001; Churazov et al. 2002; Reynolds, Heinz & Begelman 2002; Ruszkowski & Begelman 2002; Fabian 2003; Bîrzan et al. 2004; Robinson et al. 2004; Dursi & Pfrommer 2008; Fabian et al. 2008; Gitti et al. 2011). The phenomenon is likely episodic at a rate coupled to the AGN duty cycle, and total energy input when summed over the cluster lifetime can range from $\sim 10^{55}$ to 10^{61} erg. In principle, this is enough to replenish the total energy budget of ICM radiative losses for an average of the CC cluster population, although the spatial distribution and thermalization of this energy is one of several important problems that challenge the model (e.g. McNamara & Nulsen 2007, 2012, and references therein). The physics coupling AGN mechanical energy to ICM entropy remain poorly understood, and thermal conduction, gas sloshing and dynamical friction likely play additional important roles (e.g. Sparks, Macchetto & Golombek 1989; Ruszkowski & Begelman 2002; Voigt et al. 2002; Brighenti & Mathews 2003; El-Zant, Kim & Kamionkowski 2004; Soker, Blanton & Sarazin 2004; Voigt & Fabian 2004; Sparks et al. 2009; Morsony et al. 2010; Parrish, Quataert & Sharma 2010; ZuHone, Markevitch & Johnson 2010; Blanton et al. 2011; Sparks et al. 2012).

1.1 Residual cooling and star formation amid AGN feedback

Critical details of the heating and cooling feedback loop are encoded in the mass, energy and time-scale budgets of the low-temperature, high-density gas phases preferentially found in CC BCGs, such as filamentary forbidden and Balmer emission-line nebulae and $\sim 10^9$–10^{10} $M_\odot$ reservoirs of both vibrationally excited and cold[1] molecular gas (e.g. Hu, Cowie & Wang 1985; Baum 1987; Heckman et al. 1989; Jaffe & Bremer 1997; Donahue et al. 2000; Edge 2001; Jaffe, Bremer & van der Werf 2001; Edge et al. 2002; Wilman et al. 2002; McNamara, Wise & Murray 2004; Jaffe, Bremer & Baker 2005; Egami et al. 2006; Rafferty et al. 2006; Salomé et al. 2006, 2011; Wilman, Edge & Swinbank 2009; Edge et al. 2010a,b; Oonk et al. 2010; Mittal et al. 2011; Wilman et al. 2011; Lim et al. 2012).

While residual ICM condensation can contribute a major fraction of the mass budget for these phenomena (e.g. Baum 1987; Heckman et al. 1989; Cavagnolo et al. 2008; Quillen et al. 2008; Rafferty, McNamara & Nulsen 2008; O'Dea et al. 2008; Hudson et al. 2010; McDonald et al. 2010, 2011), their temperatures and ionization states are often inconsistent with the

[1] Throughout this paper, we will use 'hot' to describe $10^7 < T < 10^8$ K (X-ray bright) ICM/ISM phases, 'warm' to describe $10^4 \lesssim T < 10^5$ K [optical and ultraviolet (UV) bright] components, and 'cold' to describe $10 \lesssim T \lesssim 10^4$ K [N/M/far-infrared (FIR) bright] components. We will not discuss the critically important 10^5–10^7 K regime at great length in this paper.

$10 \lesssim T \lesssim 10^4$ K phases of a purely radiative cooling flow (e.g. Donahue & Voit 1991; Voit & Donahue 1997). Thermal conduction and suprathermal electron heating now appears to be important (Ferland et al. 2008, 2009; Sparks et al. 2009, 2012; Donahue et al. 2011; Fabian et al. 2011; Mittal et al. 2011; Oonk 2011; Johnstone et al. 2012), and a critical role is played by the clumpy and filamentary distributions of star formation ongoing amid these cold reservoirs on $\lesssim$ 30 kpc scales (e.g. Johnstone, Fabian & Nulsen 1987; Romanishin 1987; McNamara & O'Connell 1989; Hu 1992; Crawford & Fabian 1993; Allen 1995; Hansen, Jorgensen & Norgaard-Nielsen 1995; Smith et al. 1997; Voit & Donahue 1997; Cardiel, Gorgas & Aragón-Salamanca 1998; Hutchings & Balogh 2000; Mittaz et al. 2001; Oegerle et al. 2001; O'Dea et al. 2001, 2004, 2008, 2010; McNamara, Wise & Murray 2004; Hicks & Mushotzky 2005; Rafferty et al. 2006, 2008; Bildfell et al. 2008; Voit et al. 2008; Loubser et al. 2009; McDonald et al. 2010, 2011; Oonk et al. 2011).

Estimated star formation rates range from a few to tens of solar masses per year, and strongly correlate with upper limits on spectroscopically derived ICM mass deposition rates, as well as CO-inferred molecular gas masses (e.g. O'Dea et al. 2008). This suggests a direct causal connection between reduced cooling flows and star formation, as BCGs with young stellar populations are always found in CC clusters (Bildfell et al. 2008; Loubser et al. 2009). New evidence suggests that star formation occurs when multiphase clouds and filaments precipitate out of the ICM as its central entropy drops below a critical threshold ($\lesssim$20–30 keV cm^{-2}; Cavagnolo et al. 2008; Rafferty et al. 2008; Voit et al. 2008; Sharma et al. 2011; Gaspari, Ruszkowski & Sharma 2012).

But while the pathway of entropy loss from hot ambient medium to cold star-forming clouds may be strongly influenced by AGN feedback, it is not known whether residual cooling persists at constant low levels or in elevated episodes anti-correlated to the AGN duty cycle (e.g. O'Dea et al. 2010; Tremblay 2011). Moreover, models invoking radio-mode feedback to quench cooling flow signatures such as star formation must be reconciled with evidence that in several systems (e.g. Abell 1795 and Abell 2597; O'Dea et al. 2004), the propagating radio source may trigger compact, short-duration starbursts as it propagates amid a dense medium (e.g. Elmegreen & Elmegreen 1978; Voit 1988; De Young 1989; McNamara & O'Connell 1993; O'Dea et al. 2004; Batcheldor et al. 2007; Holt, Tadhunter & Morganti 2008; Holt et al. 2011). The picture is further complicated by the role played by (e.g.) thermal conduction and cold accretion scenarios like gas-rich mergers, whose importance relative to residual hot-mode ICM cooling has driven a debate that is still unsettled after three decades (e.g. Sparks et al. 1989, 2012; Holtzman et al. 1996). Advances in understanding largely rely upon multiwavelength data that sample all temperature phases of the ISM in CC BCGs, the transport processes between these phases, and their associated mass and energy budgets.

1.2 The brightest cluster galaxy in Abell 2597

To that end, in this paper we present a multiwavelength study of the archetypal CC cluster Abell 2597. New *Chandra* X-ray and *Herschel* FIR observations, combined with a vast suite of archival data, enable a radio-through-X-ray study of the ICM/ISM on the scale of its AGN feedback interaction region (i.e. its central $\lesssim$30 kpc X-ray cavity network). Abell 2597 (hereafter A2597) is an Abell (Abell 1958; Abell, Corwin & Olowin 1989) richness class 0 galaxy cluster with an X-ray surface brightness profile that is sharply peaked about its centrally dominant elliptical BCG at redshift $z = 0.0821$ (Voit & Donahue 1997). The galaxy is host to one of the nearest known compact steep spectrum (CSS; O'Dea 1998) radio sources, PKS 2322−122, which exhibits a compact (10 kpc) and bent Fanaroff–Riley class I (FR I) morphology at 8.4 GHz (Fanaroff & Riley 1974; Wright & Otrupcek 1990; Griffith & Wright 1994; O'Dea et al. 1994a; Sarazin et al. 1995).

A2597 is one of the only CC clusters with a convincing Far Ultraviolet Spectroscopic Explorer (*FUSE*) detection of [O VI] λ1032 Å emission stemming from a 10^5-10^7 K gas component (Oegerle et al. 2001), and high-resolution *XMM–Newton* X-ray spectroscopy reveals weak Fe XVII features amid a soft X-ray excess (Morris & Fabian 2005). It is therefore one of the best known candidates for harbouring a moderately powerful residual cooling flow with a mass deposition rate of $90 \pm 15\,M_\odot$ yr^{-1} within a 100-kpc cluster-centric radius (Morris & Fabian 2005). The BCG harbours a $1.8 \pm 0.3 \times 10^9\,M_\odot$ cold H_2 component, inferred from CO observations[2] (e.g. Edge 2001; Salomé & Combes 2003), as well as a young stellar component cospatial with an Hα-bright filamentary emission-line nebula (e.g. Heckman et al. 1989; Voit & Donahue 1997; Koekemoer et al. 1999; O'Dea et al. 2004; Oonk et al. 2011). These features reside amid a network of prominent X-ray cavities (McNamara et al. 2001; Clarke et al. 2005), making A2597 an ideal subject for studies of AGN/ISM interactions (Tremblay et al. 2012). For these reasons and others, A2597 enjoys a long history of cross-spectrum analysis in the literature (X-ray – Crawford et al. 1989; Sarazin et al. 1995; Sarazin & McNamara 1997; McNamara et al. 2001; Clarke et al. 2005; Morris & Fabian 2005; UV/optical – McNamara & O'Connell 1993; De Young 1995; Voit & Donahue 1997; Cardiel et al. 1998; Koekemoer et al. 1999; McNamara et al. 1999; Oegerle et al. 2001; O'Dea et al. 2004; Jaffe et al. 2005; Oonk et al. 2010, 2011; IR – McNamara & O'Connell 1993; Voit & Donahue 1997; Koekemoer et al. 1999; McNamara et al. 1999; O'Dea et al. 2004; Jaffe et al. 2005; Donahue et al. 2007, 2011; sub-mm – Edge 2001; Salomé & Combes 2003; Edge et al. 2010a,b; radio – O'Dea, Baum & Gallimore 1994b; Sarazin et al. 1995; Taylor et al. 1999; Pollack, Taylor & Allen 2005; Clarke et al. 2005).

In Section 2 we describe the new and archival multiwavelength observations used in this paper. In Section 3 we use the new *Chandra* X-ray observations to assemble an AGN feedback energy budget by using the kpc-scale cavity network as a lower limit calorimeter to the AGN kinetic energy input. In Section 4 we present new *Herschel* FIR data and use them to place constraints on the residual cooling flow. These results are used to frame a discussion on star formation, which we present in Section 5. A concluding discussion and summary are provided in Sections 6 and 7. Throughout this work, we adopt $H_0 = 71\,h_{71}^{-1}$ km s^{-1} Mpc^{-1}, $\Omega_{\rm M} = 0.27$ and $\Omega_\Lambda = 0.73$. In this cosmology, 1 arcsec corresponds to $\sim$1.5 kpc at the redshift of the A2597 BCG ($z = 0.0821$). This redshift corresponds to an angular size distance of $D_{\rm A} \approx 315$ Mpc and a luminosity distance of $D_{\rm L} \approx 369$ Mpc.

2 OBSERVATIONS AND DATA REDUCTION

Table 1 contains a summary of all new and archival observations used in this paper. We refer the reader to the publications listed in column 9 for technical information pertaining to the archival observations. The new *Chandra* X-ray observations, totalling 150 ks

[2] Updated CO-inferred molecular hydrogen mass is from P. Salomé (private communication), using unpublished IRAM (Institut de Radioastronomie Millimétrique) observations. We discuss this in Section 4.

Table 1. A summary of the new and archival observations used (directly or referentially) in this analysis. This table also applies to the analysis presented in Tremblay et al. 2012. Column (1): facility name; column (2): instrument used for observation; column (3): configuration of instrument/facility; column (4): wavelength regime/spectral line observed or filter used; column (5): exposure time; column (6): facility-specific observation or programme ID; column (7): date of observation; column (8): principal investigator (PI) of observation or programme; column (9): reference to publication where the data were first published – 1: McNamara et al. (2001); 2: Oonk et al. (2011); 3: O'Dea et al. (2004); 4: Koekemoer et al. (1999); 5: Holtzman et al. (1996); 6: Donahue et al. (2000); 7: Donk et al. (2010); 8: Donahue et al. (2007); 9: Edge et al. (2010a); 10: Edge et al. (2010b); 11: Sarazin et al. (1995); 12: Taylor et al. (1999); 13: Clarke et al. (2005). New: data first published in this paper.

Observatory (1)	Instrument (2)	Mode/config. (3)	Band/filter/line (4)	Exp. time (5)	Prog./obs. ID (6)	Obs. date (7)	Programme PI (8)	Reference (9)
			X-ray observations					
Chandra	ACIS-S	FAINT	X-ray (0.5−7 keV)	39.8 ks	922	2000 Jul 28	McNamara	1
···	ACIS-S	VFAINT	X-ray (0.5−7 keV)	52.8 ks	6934	2006 May 1	Clarke	New
···	ACIS-S	VFAINT	X-ray (0.5−7 keV)	60.9 ks	7329	2006 May 4	Clarke	New
			Far ultraviolet/optical/near-infrared observations					
HST	ACS	SBC	F150LP (FUV)	8141 s	11131	2008 Jul 21	Jaffe	2
···	STIS	FUV MAMA	F25SRF2 (Lyα)	1000 s	8107	2000 Jul 27	O'Dea	3
···	WFPC2	···	F410M	2200 s	6717	1996 Jul 27	O'Dea	4
···	WFPC2	···	F450W	2500 s	6228	1995 May 07	Trauger	5
···	WFPC2	···	F702W (*R* band)	2100 s	6228	1995 May 07	Trauger	5
···	NICMOS	NIC2	F212N	12032 s	7457	1997 Oct 19	Donahue	6
···	NICMOS	NIC2	F160W (*H* band)	384 s	7457	1997 Dec 03	Donahue	6
ESO VLT	SINFONI	···	*K* band	600 s	075.A-0074	2005 Jul/Aug	Jaffe	7
			Mid-/far-infrared observations					
Spitzer	IRAC	Mapping	3.6, 4.5, 5.8, 8 μm	3600 s (each)	3506	2005 Nov 24	Sparks	8
···	MIPS	···	24, 70, 160 μm	2160 s (each)	3506	2005 Jun 18	Sparks	8
Herschel	PACS	Photometry	70, 100, 160 μm	722 s (each)	13421871(18-20)	2009 Nov 20	Edge	9
···	SPIRE	Photometry	250, 350, 500 μm	3336 s	1342187329	2009 Nov 30	Edge	9
···	PACS	Spectroscopy	[O I] λ63.18 μm	6902 s	1342187124	2009 Nov 20	Edge	10
···	···	···	[O III] λ88.36 μm	7890 s	1342188703	2009 Dec 30	Edge	10
···	···	···	[N II] λ121.9 μm	7384 s	1342188942	2010 Jan 04	Edge	10
···	···	···	[O IB] λ145.52 μm	7382 s	1342188704	2009 Dec 30	Edge	10
···	···	···	[C I] λ157.74 μm	6227 s	1342187125	2009 Nov 20	Edge	10
···	···	···	[Si I] λ68.47 μm	11834 s	1342210651	2010 Dec 01	Edge	New
			Radio observations					
NRAO VLA	···	A array	8.44 GHz	15 min	AR279	1992 Nov 30	Roettiger	11
···	···	A array	4.99 GHz	95 min	BT024	1996 Dec 7	Taylor	12, 13
···	···	A array	1.3 GHz	323 min	BT024	1996 Dec 7	Taylor	12, 13
···	···	A array	330 MHz	180 min	AC647	2003 Aug 18	Clarke	13
···	···	B array	330 MHz	138 min	AC647	2002 Jun 10	Clarke	13

(128 ks flare-free) in combined effective exposure time, were reduced using the standard CIAO v4.2 threads with v4.3.1 of the calibration data base. More details can be found in Tremblay et al. (2012), which presents the spatial and spectral analysis of these new observations.

Herschel Space Observatory observations of A2597 were obtained in 2009 November with the Photodetector Array Camera and Spectrometer (PACS), as well as the Spectral and Photometric Imaging Receiver (SPIRE). These observations were part of an Open Time Key Project (OTKP) investigating the FIR line and continuum properties of a sample of 11 BCGs in well-known X-ray and optical line selected CC clusters (PI: A. Edge, 140 h). Preliminary results for A2597 have been published in the works submitted as part of the science demonstration phase (Edge et al. 2010a,b). The data were processed with the *Herschel* Interactive Processing Environment (HIPE) package version 7.1.0. See Edge et al. (2010a,b), Mittal et al. (2011) and Oonk et al. (in preparation) for details on the data reduction. The present paper uses PACS and SPIRE data to fill in critical gaps in the FIR spectral energy distribution (SED) for A2597, enabling constraints on dust masses and temperatures. The [O I] λ68.4 μm PACS observation, because it is at high spectroscopic resolution, is also used to place constraints on the cold gas kinematics.

3 AGN FEEDBACK ENERGY BUDGET

Kiloparsec-scale X-ray cavities can be used as lower limit calorimeters on the kinetic energy associated with AGN outflows, and the duty cycle over which these outbursts occur (e.g. Churazov et al. 2002; Bîrzan et al. 2004; Dunn & Fabian 2006; Rafferty et al. 2006; McNamara & Nulsen 2007, 2012; Fabian 2012). A study of the original 40-ks *Chandra* observation by McNamara et al. (2001) and Clarke et al. (2005) (hereafter M01 and C05, respectively) revealed western and north-eastern ghost cavities in A2597. The new 150-ks *Chandra* data reveal the cavity network to be more extensive than originally thought, changing the interpretation of the AGN feedback energy budget and outburst history. We discuss these two new results in this section.

3.1 The X-ray cavity network

In Fig. 1 we present the combined 150-ks 0.5–7 keV X-ray data from Tremblay et al. (2012). All panels are aligned with an identical

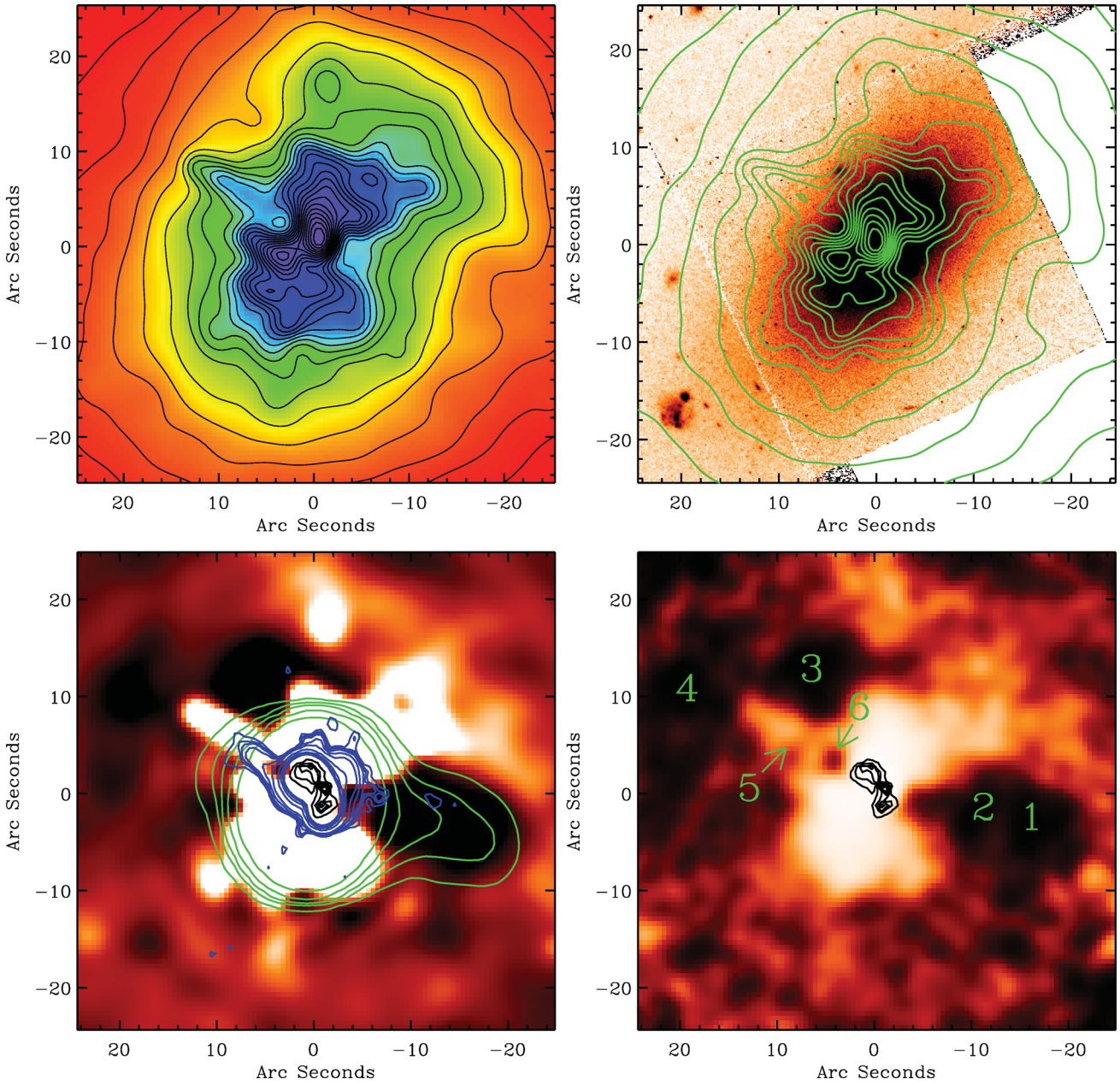

Figure 1. Top left: exposure-corrected 0.5–7 keV image of the three merged *Chandra* observations (see Table 1). The data have been smoothed with an adaptive Gaussian kernel. Black contours are overlaid to better show the spatially anisotropic nature of the emission. The innermost contour marks a flux of 4.6×10^{-7} photons s^{-1} cm^{-2} pixel^{-1}, and the contours move outwards with a flux decrement of 2.0×10^{-8} photons s^{-1} cm^{-2} pixel^{-1}. Top right: the same 0.5–7 keV X-ray contours (in green), overlaid on the broad-band *HST*/WFPC2 F702W (*R*-band) exposure of the A2597 BCG (shown in orange). Note that the anisotropy of the X-ray emission is largely confined to the inner regions of the galaxy. Bottom left: unsharp mask of the X-ray data, made by subtraction of a 20-arcsec Gaussian smoothed version from the adaptively smoothed version. 330-MHz VLA contours have been overlaid in green, while the 1.3-GHz radio contours are plotted in blue, and the 8.4-GHz radio contours appear in black. bottom right: unsharp mask made by subtracting the same 20-arcsec Gaussian smoothed version of the image from a 5-arcsec Gaussian smoothed version, then dividing by the sum of the two images. The major (10σ excess or deficit) morphological features which will be the subject of further spatial analysis in this paper have been labelled 1–6. The colour schemes of the two bottom panels show regions of X-ray surface brightness excess in red/orange, while deficits (cavities) appear in black. All panels share an identical field of view, centred at RA = $23^{\rm h}25^{\rm m}19\overset{\rm s}{.}75$ and Dec. = $-12^\circ07'26\overset{''}{.}9$ (J2000).

50×50 arcsec^2 (75×75 kpc^2) field of view (FOV) centred on the X-ray centroid at RA = $23^{\rm h}25^{\rm m}19\overset{\rm s}{.}75$ and Dec. = $-12^\circ07'26\overset{''}{.}9$ (J2000). East is left and north is up. The top left panel shows the exposure-corrected, merged data adaptively smoothed with a variable width Gaussian kernel whose radius self-adjusts to match the local event density. Black surface brightness contours are overlaid to make individual features easier to view. The innermost contour marks a flux of 4.6×10^{-7} photons s^{-1} cm^{-2} pixel^{-1}, and the contours move outwards with a decrement of 2.0×10^{-8} photons s^{-1} cm^{-2} pixel^{-1}.

In the top right panel of Fig. 1 we overlay the adaptively smoothed X-ray contours on the *Hubble Space Telescope* (*HST*) Wide Field Planetary Camera 2 (WFPC2) *R*-band observation of the A2597 BCG (shown in red/orange). Note that the anisotropy of the X-ray

emission is confined to the scale of the BCG, while the outermost regions assume a smoother, more elliptical shape. The major axes of the X-ray and BCG stellar isophotes are aligned.

In the bottom two panels of Fig. 1 we show the same 0.5–7 keV data processed in two ways: (1) a highly processed unsharp mask made by subtracting a 30-arcsec Gaussian smoothed image from the adaptively smoothed image shown in Fig. 1 (top left), and (2) a more conventional unsharp mask made by subtracting a 20-arcsec Gaussian smoothed image from a 5-arcsec (non-adaptive) Gaussian smoothed version. The subtracted data are then divided by the sum of the two images. Regions of X-ray surface brightness excess over the subtracted smooth background appear in white, while deficits (cavities) appear in black. 8.4-GHz, 1.3-GHz and 330-MHz Very Large Array (VLA) radio contours from Sarazin et al. (1995), Taylor et al. (1999) and C05 are overlaid on the bottom left panel. See section 3.2 of Tremblay et al. (2012) for a discussion of the strong radio/X-ray spatial correlations that are evident in this figure. We note that these unsharp mask edge enhancement methods (particularly method 1) are inherently noisy, and introduce artefacts that complicate a quantitative morphological analysis. The significance of the observed features must therefore be estimated from the un-processed data. We show these mostly as viewing aids for the X-ray cavities discussed in this section. We do note that the processed images shown here do not significantly differ in apparent morphology from the un-processed raw *Chandra* data that can be seen in fig. 2 of Tremblay et al. (2012).

In the bottom right panel of Fig. 1 we label the six features that are associated with $\gtrsim 10\sigma$ deficits or excesses relative to the local mean. The significance of these features was estimated by comparing unsmoothed counts in like-sized regions at the same cluster-centric radius. Throughout this paper we refer to these features with a common label and name. These are: (1) the 'M01 western ghost cavity', (2) the 'C05 X-ray tunnel', (3) the 'M01 northern ghost cavity', (4) the 'eastern ghost cavity', (5) the 'cold filament' and (6) the 'C05 filament base cavity'. For clarity, these names and labels will be used consistently throughout this paper. Feature (2), the 'cold filament', is discussed in section 5 of Tremblay et al. (2012) in the context of AGN/ISM interactions and multiphase gas dredge-up by the radio source.

While (for 'historical' reasons) we label features (1) and (2) independently, our deeper data make it clear that western ghost cavity described by M01 and C05 is part of a larger 'teardrop' shaped cavity $\sim$25 kpc in projected length (C05 originally suggested this in their discussion of an 'X-ray tunnel'). This changes the interpretation of the AGN outburst history (relative to the conclusions drawn in M01), which we will discuss below. So as to enable comparison with past papers (e.g. M01; Bîrzan et al. 2004; Rafferty et al. 2006) that have treated the M01 cavity as a separate feature, we maintain independent labels (1 and 2) for the cavity and tunnel. We stress that these features are part of one larger cavity, which we will label '1+2' and call the 'western large cavity' for the remainder of this paper.

3.2 Age dating the X-ray cavities

We adopt the simple model used by Bîrzan et al. (2004) and Rafferty et al. (2006) in estimating rough ages for the X-ray cavities, assuming their density is very low relative to the ambient gas density. Three time-scales can be considered, the most simple of which assumes that the bubble rises in the plane of the sky at the sound speed $c_{\rm s} \simeq \sqrt{kT/\mu m_{\rm p}}$, where $\mu = 0.62$ is the mean molecular weight in units of the proton mass, $m_{\rm p}$. If the bubble is at projected cluster-centric radius R, then this sonic rise time-scale is given by

$$t_{c_{\rm s}} \simeq R/c_{\rm s}. \quad (1)$$

As the initial stages of cavity inflation are thought to be supersonic, followed by subsonic buoyant rise, this simple approach may best reflect an average of the two phases. Alternatively, if the supersonic inflation period is a negligible fraction of the cavity's age and drag forces limit the cavity's terminal velocity $v_{\rm t}$, the buoyant time-scale can be written as

$$t_{\rm buoy} \simeq \frac{R}{v_{\rm t}} \simeq R\sqrt{\frac{AC}{2gV}}, \quad (2)$$

where g is the local gravitational acceleration, V is the cavity volume, A is its cross-sectional area and $C = 0.75$ is the drag coefficient adopted from Churazov et al. (2001) by e.g. Bîrzan et al. (2004). Finally, cavity ages can be constrained by estimating the time required to refill the volume displaced by a bubble of radius r as it rises a height equal to its diameter,

$$t_{\rm refill} \simeq 2R\sqrt{\frac{r}{GM\,(<R)}} = 2\sqrt{\frac{r}{g}}, \quad (3)$$

where $M(<R)$ is the mass enclosed within a sphere of radius R.

Bîrzan et al. (2004) made all three estimates for the NE and W ghost cavities in A2597 (features 1 and 3 in Fig. 1, bottom right panel), using the early short (40 ks) *Chandra* observation. So as to provide an independent check of their results using the deeper X-ray data, we follow their procedure almost exactly, and repeat their calculations for the M01 ghost cavities, the western large cavity (features 1 and 2), as well as the newly detected cavities (4) and (6) (as labelled in Fig. 1). Like Bîrzan et al. (2004), we adopt the A2597 BCG stellar velocity dispersion of $\sigma \approx 224 \pm 19\,{\rm km\,s^{-1}}$ from Smith, Heckman & Illingworth (1990) in our calculation of the local gravitational acceleration g:

$$g \simeq \frac{2\sigma^2}{R}, \quad (4)$$

assuming that the galaxy is an isothermal sphere. In Tremblay et al. (2012) we calculate a local value for g by estimating the total enclosed gravitating mass from a β-model fitted to the X-ray surface profile. For this discussion however, it is sufficient to adopt the Bîrzan et al. (2004) method for estimating g (the two methods turn out to be roughly consistent at the radius of the X-ray cavity network anyway). Unlike Bîrzan et al. (2004), we use kT inferred from the cavity positions on the X-ray temperature map presented in Tremblay et al. (2012) to calculate the sound speed in the X-ray gas. We use the 2D temperature map in lieu of the 1D radial temperature profile because A2597 is azimuthally anisotropic in X-ray temperature (not to mention surface brightness) on these scales. Furthermore, in calculating the pV work associated with each cavity, we use the projected density profile to estimate the pressure nkT at the cluster-centric radius of each cavity.

The results of these calculations are given in Table 2. Our findings are roughly consistent with those of Bîrzan et al. (2004). For example, in age dating the M01 western ghost cavity we find $t_{c_{\rm s}} \approx 27$ Myr, $t_{\rm buoy} \approx 88$ Myr and $t_{\rm refill} \approx 66$ Myr, while Bîrzan et al. (2004) find 26, 66 and 86 Myr, respectively. None of these estimates accounts for projection effects, and all assume that the bubble rises purely in the plane of the sky. This results in an underestimation of the cavity age by generally less than a factor of 2 (Bîrzan et al. 2004; Rafferty et al. 2006; McNamara & Nulsen 2007).

Table 2. Spatial properties and energetics of the X-ray cavities. Column (1): label of morphological feature that corresponds to that assigned in the lower right panel of Fig. 1; column (2): name given to the corresponding feature; column (3): projected radial distance (length) of the feature from the radio core to the estimated centre (edge) of the feature; column (4): estimated radius of the feature; column (5): estimated work associated with cavity assuming subsonic inflation; column (6): age of the cavity if it rises at the local sound speed; column (7): buoyant, subsonic cavity rise time; column (8): time needed to refill the displaced cavity volume; column (9): X-ray cavity power, assuming the cavity is filled with relativistic plasma. See Section 3 for more details on these calculations.

Label (1)	Name (2)	R (D) (kpc) (3)	r (kpc) (4)	pV ($\times 10^{57}$ erg) (5)	t_{c_s} ($\times 10^7$ yr) (6)	$t_{\rm buoy}$ ($\times 10^7$ yr) (7)	$t_{\rm refill}$ ($\times 10^7$ yr) (8)	$P_{\rm cav}$ ($\times 10^{42}$ erg s^{-1}) (9)
1+2	Western 'large cavity'	9	9	35.9	1.0	1.4	5.6	170.6
3	M01 northern 'ghost' cavity	21	6.6	7.0	2.7	6.1	7.3	16.5
4	Eastern 'ghost' cavity	35	3.6	0.79	3.8	17.8	6.9	1.05
6	Filament base cavity	9	2.3	0.30	1.1	2.7	2.8	1.73

3.3 Cavity heating energy reservoir

In column 9 of Table 2 we calculate the mean instantaneous power of each cavity $P_{\rm cav}$,

$$P_{\rm cav} = \frac{4pV}{\langle t \rangle}, \quad (5)$$

where $\langle t \rangle$ is the average of the cavity ages listed in columns 6–8. We have assumed the cavities are filled with a relativistic plasma, such that their enthalpy can be approximated as $4pV$ (e.g. McNamara & Nulsen 2007).

The total sum of all cavity thermal energies (pV) listed in column 5 is 4.4×10^{58} erg. This serves as a rough, lower limit estimate on the kinetic energy injected by the AGN into the ambient X-ray gas during the (a) current AGN episode or perhaps (b) during the past two or more episodes of activity. This is close to the inferred mechanical energy of the central 8.4-GHz radio source, which Sarazin et al. (1995) estimated to be 9×10^{57} erg. In principle, the roughly estimated mechanical input from the radio source could be capable of accounting for the energy budget inferred from the X-ray cavities, ignoring time-scale arguments. Whether or not these cavities have been produced by one or more AGN episodes is the subject of the following section.

3.4 The AGN duty cycle and heating time-scale budget

A network of multiple cavities found at varying cluster-centric radii (as we find in A2597) may be produced with an episodically varying AGN, transitioning between either 'on' and 'off' or high and low modes. Cycling times between the triggering of radio activity, the onset of quiescence and the subsequent re-ignition of activity are typically estimated to be of the order of 10^7-10^8 yr in general (e.g. Parma et al. 1999; Best et al. 2005; Shabala et al. 2008; Tremblay et al. 2010), and synchrotron losses limit radio source lifetimes to $\sim 10^8$ yr, unless there has been re-acceleration of the electron population. Alternatively, a steady-state AGN with a duty cycle near 100 per cent can also produce a series of discrete cavities (rather like a fish tank aerator or a dripping faucet; e.g. Peterson & Fabian 2006; McNamara & Nulsen 2007). In this section we attempt to distinguish between these two possibilities.

Based on synchrotron loss time-scales, C05 estimated the minimum energy, lower limit lifetime of the 330-MHz source (green contours in the bottom left panel of Fig. 1) to be in the range of $t_{330\,\rm MHz} \gtrsim 8 \times 10^6$ yr (if the spectral index is steep down to 10 MHz) to $t_{330\,\rm MHz} \gtrsim 5 \times 10^7$ yr (if the spectral index flattens beyond 330 MHz). This model assumes equal cosmic ray and magnetic field energy densities (equipartition), a steep spectral index of -2.7 between 1.3 GHz and 330 MHz, and that the source is a uniform prolate cylinder with a filling factor of unity. This model yields a minimum energy magnetic field strength of 29 μG and a non-thermal pressure of 5×10^{-11} dyn cm^{-2}. We note that equipartition may be a less-than-ideal assumption in this case (e.g. Fabian et al. 2002). Furthermore, deeper multiband radio observations are required to better assess the spectral index of the source across the western large cavity.

The lower end of the 330-MHz lifetime range quoted above ($t_{330\,\rm MHz} \gtrsim 8 \times 10^6$ yr) is significantly shorter than the estimated buoyant rise time of the western large cavity it fills (see Table 2, column 7). If we assume that this is the actual age of the source, and further assume that the estimated age of the western large cavity is roughly correct, then we require (a) in situ re-acceleration of electrons in the cavity or (b) a new episode of activity to feed the plasma into an already pre-established cavity (which, if empty, should collapse on a sound-crossing time $\lesssim 10^7$ yr). As we will elaborate upon below, there is little supporting evidence favouring either of these scenarios.

A 'radio source younger than the cavity' scenario could also be possible if adiabatic and/or inverse Compton losses dominate over the synchrotron processes, which would result in the radio source fading on a time-scale shorter than the synchrotron lifetime. The importance of these processes relative to synchrotron losses depends on the B field strength and unknown details of how the radio source fills the bubble. Inverse Compton losses become more efficient than synchrotron losses when the B field is extremely weak ($B < 1$ μG; e.g. Fabian et al. 2002), and adiabatic losses are not likely a limiting factor because the western large cavity is likely rising at less than the sound speed (note the absence of any detected fast shocks in the X-ray data; e.g. Tremblay et al. 2012). We therefore consider this scenario unlikely.

The upper end of the minimum-energy synchrotron lifetime is $t_{330\,\rm MHz} \gtrsim 5 \times 10^7$ yr (which itself is merely a lower limit). The 330-MHz radio source could therefore easily be roughly of the same age as the cavity it fills. This is the simplest scenario, as it is assumed that the propagation of the radio source amid the X-ray gas is the mechanism that excavates the cavity. Even if the equipartition and spectral index assumptions mean that this estimated lifetime is wrong, pressure equilibrium between the radio source and the ambient hot gas can be assumed to estimate a very similar $\sim 10^7$ yr minimum age (e.g. Fabian et al. 2002). Considering the high uncertainties associated with age dating both cavities and radio sources, (not to mention projection effects), we suggest that the western large cavity was created by the current, ongoing episode of AGN activity.

Considering the above, we cannot rule out the possibility that the AGN in A2597 is on nearly ∼100 per cent of the time. The oldest cavity (i.e. feature 4, with an estimated age of 1.8×10^8 yr) may indeed be associated with a previous epoch of AGN activity, but it could also be a detached bubble excavated by the current episode (the available data do not permit us to discriminate between these possibilities). We note that the position angle of the 8.4-GHz radio lobes is significantly offset from the western large cavity, 330-MHz and 1.3-GHz radio source (Fig. 1), and the Very Long Baseline Array (VLBA) small-scale (∼50 pc) jet axis (Taylor et al. 1999). We find it unlikely that the offset is due to the 8.4-GHz source being associated with a previous epoch of activity, considering its steep spectrum (O'Dea et al. 1994b; Clarke et al. 2005), estimated minimum-energy age of $>5 \times 10^6$ yr (Sarazin et al. 1995), and alignment of the VLBA (<50 pc) and 330-MHz (>25 kpc) major axes (Tremblay et al. 2012). Several past studies have suggested that the bend is due to the interaction of the radio source with the ambient dense gaseous medium, either by deflection or back-flow along pre-established pressure gradients (e.g. Sarazin et al. 1995; Koekemoer et al. 1999; O'Dea et al. 2004; Clarke et al. 2005; Oonk et al. 2010).

3.5 Black hole accretion rate

If the AGN is indeed nearly steady state, the central black hole (BH) requires a stable supply of gas from the ambient accretion reservoir. Assuming a mass-to-energy conversion efficiency of $\epsilon = 0.1$ (Wise et al. 2007), and assuming that the energy associated with the X-ray cavities is provided by the AGN, the sum of mean instantaneous cavity powers ($P_{\rm cav}$) requires a time-averaged BH accretion rate of

$$\dot{M}_{\rm acc} \sim \frac{P_{\rm cav}}{\epsilon c^2} \sim 0.003 - 0.03 \left(\frac{\epsilon}{0.1}\right)^{-1} {\rm M}_\odot\ {\rm yr}^{-1}, \quad (6)$$

where c is the speed of light. Using the $M_{\rm BH}$–σ relation (Magorrian et al. 1998; Ferrarese & Merritt 2000; Gebhardt et al. 2000) with the K-band host luminosity and stellar velocity dispersion yields a rough BH mass estimate of $\sim 3 \times 10^8\ {\rm M}_\odot$, for which the corresponding Eddington accretion rate would be $\sim 10\ {\rm M}_\odot\ {\rm yr}^{-1}$ (Rafferty et al. 2006). This suggests that the accretion rate, if steady, is strongly sub-Eddington, consistent with past results even for very powerful AGN (e.g. Hydra A; Wise et al. 2007). If the AGN is instead strongly variable or episodic, then gas transport to the BH could be non-steady and the actual accretion rate could vary.

3.6 There is enough energy to quench a classical cooling flow

We calculate the classical X-ray derived cooling time for A2597,

$$t_{\rm cool} \equiv \frac{5}{2} \frac{nkT}{n^2 \Lambda}, \quad (7)$$

where n and kT are respectively the gas density and temperature profiles obtained by Tremblay et al. (2012), and Λ is the $T > 0.02$ keV portion of the cooling function from Sutherland & Dopita (1993), using the generalization from Tozzi & Norman (2001).

We find that the cooling time at the $\lesssim$30 kpc outermost radius of the X-ray cavity network is ∼300 Myr. The instantaneous cooling luminosity associated with the uninhibited cooling flow (with no heating) can be calculated from the classical uninhibited mass deposition rate $\dot{M}_{\rm cool}$ using

$$L_{\rm cool} = \frac{5}{2} \frac{\dot{M}_{\rm cool}}{\mu m_{\rm p}} kT_{\rm vir}, \quad (8)$$

where $T_{\rm vir}$ is the virial temperature of the cluster. Classical mass deposition rates for A2597 range from ∼100 to $500\ {\rm M}_\odot\ {\rm yr}^{-1}$ over a range of cluster-centric radius spanning ∼30−100 kpc (e.g. Allen et al. 2001; McNamara et al. 2001; Morris & Fabian 2005). Taking a cluster virial temperature of $kT_{\rm vir} = 3.5$ keV, we find that the corresponding range of cooling luminosity is roughly $L_{\rm cool} \approx (1-4) \times 10^{44}$ erg s^{-1}. The rough sum of mean instantaneous cavity powers (see Section 3.3 and column 9 of Table 2) is $P_{\rm cav} \approx 2 \times 10^{44}$ erg s^{-1}, suggesting that, in principle, there is enough enthalpy associated with the current cavity network to offset the bulk of radiative losses and effectively quench the cooling flow.

The same conclusion holds if we estimate the predicted cooling flow luminosity directly from the new *Chandra* data, using lower limit temperatures derived from spectral fits (i.e. the MKCFLOW model $kT_{\rm low}$ values in table 1 of Tremblay et al. 2012). This is a rough, order-of-magnitude assumption which neglects many important considerations such as how this enthalpy might be dissipated and distributed in the ambient gas. Our finding that the X-ray cavities are associated with enough energy to inhibit the predicted classical cooling flow luminosity is consistent with previous results (Bîrzan et al. 2004; Dunn & Fabian 2006).

4 NEW EVIDENCE SUPPORTING A RESIDUAL COOLING FLOW MODEL FOR A2597

In the previous section, we estimated that the X-ray cavity network is associated with enough enthalpy to (in principle) replenish a significant fraction of the radiative losses associated with a classical cooling flow. However, the warm and cold gas phases in the A2597 BCG strongly suggest that some cooling from the ambient X-ray atmosphere has managed to persist, even amid AGN heating. We discuss this possibility here.

4.1 How might cooling persist amid AGN feedback?

As mentioned in Section 1, results from *XMM–Newton* and *FUSE* are consistent with a moderately strong residual (sometimes called 'reduced') cooling flow with a mass deposition rate of $\sim 30 \pm 15\ {\rm M}_\odot\ {\rm yr}^{-1}$at ∼30 kpc to $90 \pm 15\ {\rm M}_\odot\ {\rm yr}^{-1}$ at ∼100 kpc (Oegerle et al. 2001; Morris & Fabian 2005). The cooling luminosity associated with this residual cooling flow is $L_{\rm Cool,Resid} \approx (0.3\text{–}1) \times 10^{44}$ erg s^{-1}. As with 15–30 per cent of CC BCGs (depending on the sample; e.g. Salomé et al. 2006), the A2597 BCG harbours a substantial $1.8 \pm 0.3 \times 10^9\ {\rm M}_\odot$ reservoir of cold H_2 (inferred from CO observations) within its central 30 kpc (Edge 2001; Salomé & Combes 2003; P. Salomé, private communication). If the bulk of the mass budget for this cold gas is supplied by the residual cooling flow (rather than e.g. a merger), then AGN feedback cannot establish an impassable entropy floor, and some cooling to <100 K must be permitted even if there is enough energy in principle to quench the classical cooling flow. We consider four possibilities:

(i) Low levels of residual cooling persist even while AGN feedback is heating the ambient environment;

(ii) cooling occurs in a spatially structured manner, away from those regions which are being locally heated by e.g. buoyant cavities and sound waves;

(iii) cooling occurs in episodes which correspond to the times when the BH is inactive, or transitioning between active and inactive states or between high and low modes;

(iv) the substantial cold gas reservoir in the A2597 BCG stems from something other than a cooling flow, i.e. one or more gas-rich mergers.

These are not the only possibilities, and several or all of the four scenarios listed above could work in tandem.

As discussed in Section 3.4, we cannot rule out the possibility that the AGN duty cycle in A2597 is close to 100 per cent. Even if this is not the case, and the AGN is episodic over 10^7 yr periods, a cavity's enthalpy reservoir should be dissipated as heat in the ISM/ICM on a time-scale of the order of the cavity lifetime (Churazov et al. 2002; Reynolds et al. 2002; Bîrzan et al. 2004; Dunn & Fabian 2006). The net effect of this time buffer could be that ISM/ICM heating rates are roughly constant in time for cavity heating models, even if the AGN itself is episodic over these time-scales. If we assume that this is correct, and further assume that most cold baryons in the nucleus cooled from the hot atmosphere, then we might conclude that low levels of residual cooling must persist at a roughly constant rate. This would be consistent with scenario (i) or (ii) above. In this case, a near-constant cooling rate would funnel a steady flow of gas to the BH accretion reservoir, fuelling a long-lived rather than episodic AGN. This would be consistent with our suggestion that the AGN in A2597 is approximately steady state. We would require inhomogeneous heating and cooling (e.g. scenario ii, iii and/or iv) to allow cooling to re-trigger the radio source.

The notion that cooling could proceed in a spatially discrete and structured manner (scenario ii) is not controversial, and was predicted even by the earliest cooling flow models (see e.g. the review by Fabian 1994). While long-lived sound waves could theoretically heat the outermost regions of cool cores in a more homogeneous manner, heating by short-lived X-ray cavity enthalpy dissipation is expected to be spatially confined to the scale and location of the cavity, regardless of the Reynolds number of the plasma (see e.g. the review by McNamara & Nulsen 2007). In this case, one would expect cooling to proceed in the regions unaffected by local heating. Recently, deep X-ray observations of Perseus and A2146 by (respectively) Fabian et al. (2011) and Russell et al. (2012) revealed bright X-ray filaments which alone could be associated with a significant fraction ($\lesssim$80 per cent) of the total inferred cooling rate. In Section 5 of this paper, we will show a similar result for A2597.

On the other hand, O'Dea et al. (2010) studied a sample of seven CC BCGs selected on the basis of an IR excess associated with elevated star formation rates, and found that each tended to possess a weak, compact radio source. The combination of higher SFR and lower radio power may be consistent with a scenario wherein a low state of AGN feedback allows for increased residual condensation from the ambient X-ray atmosphere, accounting for the elevated star formation rates. This would be consistent with scenario (iii), though A2597 does not appear to be a strong candidate. We stress that scenarios (i)–(iii) are not contradictory or competitive with one another, and each could play a simultaneously important role. The same is true for possibility (iv), which we investigate in more detail below.

4.2 New results on cold gas kinematics – discriminating between hot and cold accretion scenarios

The new *Chandra* and *Herschel* data can be used to better understand the origin of the $1.8 \pm 0.3 \times 10^9$ M$_\odot$ cold reservoir in A2597. Relative to BCGs in non-CC clusters, CC BCGs are far more likely to harbour central emission-line nebulae, cold gas components and radio sources (e.g. Mittal et al. 2009; Hudson et al. 2010, and references therein). This strong circumstantial evidence suggests a causal connection between these warm/cold phenomena and residual condensation from the ICM, but the literature has so far not reached consensus as to the relative importance of gas-rich major and minor mergers in this relationship (e.g. Sparks et al. 2012). Koekemoer et al. (1999), for example, suggest that some physical features of the A2597 emission-line nebula are consistent with what might be expected from a gas-rich minor merger. The BCG stellar isophotes do not show any obvious signs of disturbance, so a recent major merger is likely ruled out, at least within the past several dynamical times.

In Fig. 2 we plot the [O I] λ63 μm line profile from the *Herschel* PACS spectroscopy (Edge et al. 2010b) in black, over the CO(2−1) rotational line profile (in blue) from the IRAM 30-m observations of A. Edge & P. Salomé (private communication, data previously unpublished). [O I] λ63 μm is one of the primary atomic coolant lines for $T \lesssim 40$ K gas (Kaufman et al. 1999), and CO(2−1) can be considered a tracer of the molecular hydrogen reservoir. Following Solomon et al. (1997) and adopting a standard Milky Way (MW) H_2 mass-to-CO luminosity ratio of $\alpha = 4.6\,M_\odot\,(K\,km\,s^{-1}\,pc^2)^{-1}$, the CO line luminosity of $L'_{CO} = 3.9 \times 10^8\,K\,km\,s^{-1}\,pc^2$ converts to a CO-inferred molecular hydrogen mass of $M_{H_2} = 1.8 \pm 0.3 \times 10^9\,M_\odot$.

[O I] was detected at a signal-to-noise ratio (S/N) of $\gtrsim$30 but unresolved (the *Herschel* beam at this wavelength is ∼9 arcsec ≈ 13.5 kpc). The [O I] line is centred at the systemic BCG redshift, and has an intrinsic full width at half-maximum (FWHM) of 405 ± 55 km s^{-1} with a possible asymmetric red velocity excess offset from the systemic velocity by ∼+ 250 km s^{-1}. The CO(2−1) FWHM is slightly narrower (300 ± 50 km s^{-1}) though the profile may also exhibit a scaled down signature of the same red asymmetry (Edge et al. 2010b). The IRAM 30-m CO(2−1) beam is 13 arcsec ≈ 20 kpc, larger than the *Herschel* 63-μm beam, so a red wing arising from gas near the centre would be more diluted in the CO(2−1) profile. A very marginal (2.6σ) CO(1−0) detection was also obtained by A. Edge & P. Salomé at the same velocity as the

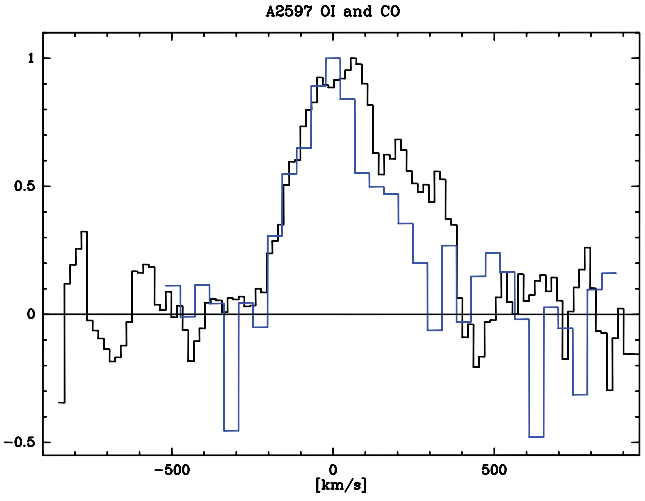

Figure 2. A comparison of the *Herschel* [O I] λ63 μm line profile, in black, with the IRAM 30-m CO(2−1) rotational line profile in blue. The [O I] line is centred at the systemic BCG redshift, and has an intrinsic FWHM of 405 ± 55 km s^{-1} with a possible asymmetric red velocity excess offset from the systemic velocity by ∼+250 km s^{-1}. The CO(2−1) FWHM is slightly narrower (300 ± 50 km s^{-1}), and may also exhibit a slight red asymmetry. The spectral resolution of the CO data is 45 km s^{-1}. Both spectra have been normalized to their maximum to enable comparison of the line profiles. Intensities are therefore arbitrary.

CO(2−1) line, suggesting that the CO(1−0) data are beam diluted. This means that the CO is probably concentrated in a region smaller than 11 arcsec (17 kpc). The CO line ratio (if correct) is close to or larger than 4, suggesting this as well. O'Dea et al. (1994b) detected an unresolved narrow H I absorption component in the nucleus with an FWHM of $\sim 220 \pm 10$ km s^{-1}, as well as a broader component spatially resolved on the scale of the 8.4-GHz radio lobes with an FWHM of $\sim 412 \pm 40$ km s^{-1}, consistent with the *Herschel* results.

Donahue et al. (2000) detected H_2 1−0 *S*(3) 2.2-μm emission stemming from vibrationally excited molecular hydrogen on roughly the same spatial scale, with some resolved morphology tracing the optical emission-line filaments. The emission is far too bright to be directly accounted for by a cooling flow, and UV irradiation by the young stellar component was the only model capable of accounting for both the Hα/H_2 line ratios, as well as the FUV continuum strength. That study ruled out AGN photoionization, fast and slow shocks and X-ray heating as the dominant ionization source. Excitation by non-thermal electrons may play an important role (Ferland et al. 2009). Jaffe et al. (2005) and Oonk et al. (2010) have detected molecular gas out to a maximal radius of ∼20 kpc northwards of the nucleus. Thus far, this is the largest known radial extent at which a tracer of the warm/cold ISM has been detected in A2597 (the longest CC BCG optical filaments have been detected out to ∼50 kpc, for Perseus/NGC 1275; e.g. Conselice, Gallagher & Wyse 2001; Fabian 2003; Hatch et al. 2006). This does not imply that there is no warm/cold gas beyond this boundary, as all of these observations are limited by sensitivity. The average velocity profiles for the ionized and molecular gas, studied by Oonk et al. (2010) using European Southern Observatory (ESO) Very Large Telescope (VLT) Spectrograph for INtegral Field Observations in the Near Infrared (SINFONI) data (see Table 1), are comparable to one another and are centred at roughly the systemic velocity. The data show smaller scale velocity (and velocity dispersion) excesses that appear to be associated with the propagation of the radio source (Tremblay et al. 2012).

Gas cooling from an ambient X-ray atmosphere should be associated with low net angular momentum. Its velocity profile should therefore smoothly increase from the systemic velocity at larger radii (e.g. ∼50 kpc) to a few hundred km s^{-1} in the centre of the BCG. As discussed above, this is consistent with what has so far been observed. On the other hand, cold gas acquired through a merger may be associated with higher net angular momentum and exhibit bulk rotation at larger radii. The relative consistency of the [O I], CO(2−1), H I and H_2 velocity profiles seems consistent with what would be expected if residual ICM cooling deposited these gaseous components into the BCG with low excess angular momentum or velocity structure. While we cannot speak of the velocity structure of the X-ray gas on these scales, the fact that the X-ray isophotes are consistently elongated along the major axis of the BCG (top right panel of Fig. 1) supports the notion that the two components are roughly similar in terms of angular momentum.

Alternatively, a merger origin for the gas cannot be ruled out. Although high-velocity gas is not detected at large radii, and although the cold gas is concentrated in the very inner regions of the nucleus without complex or high amplitude velocity structures, one can imagine a merger producing similar results if enough time has passed since the merger for the gas to reach the nucleus and couple with the local dynamics. A possible merger origin for the warm/cold gas phases in A2597 is discussed in detail by Koekemoer et al. (1999).

A purely merger-based origin for this gas would be difficult to reconcile with the *FUSE* and *XMM–Newton* results consistent with cooling gas $<10^6$ K, unless conductive interfaces produce the lines attributed to cooling (e.g. Sparks et al. 2012). The observed star formation X-ray cooling time threshold (Cavagnolo et al. 2008; Rafferty et al. 2008), which we will discuss in Section 5, would also be difficult to understand in a 'mergers only' scenario. In the sections below, we will argue that ICM contributions likely play a very significant role in A2597, regardless of the unknown contribution by cold gas acquisition scenarios like mergers. We reiterate that a recent gas-rich major merger is almost certainly ruled out for A2597.

4.3 New *Herschel* constraints on the cold gas and dust components

The $1.8 \pm 0.3 \times 10^9$ M$_\odot$ cold molecular gas reservoir in A2597 is cospatial with the ∼10-kpc emission-line nebula, which has been studied extensively in the literature (e.g. Heckman et al. 1989; McNamara & O'Connell 1993; Voit & Donahue 1997; Koekemoer et al. 1999; McNamara et al. 1999; Oegerle et al. 2001; O'Dea et al. 2004; Jaffe et al. 2005; Oonk et al. 2011). High spatial resolution archival *HST* imaging, shown in Fig. 3, reveals its complex filamentary morphology in the FUV and optical (panels a–d of Fig. 3). Deep optical spectroscopy by Voit & Donahue (1997) shows the gas temperature, abundance and electron density of the nebula to be 9000–12 000 K, ∼0.5 Z$_\odot$ and $n_e \sim 200$ cm^{-3}, respectively. Koekemoer et al. (1999) estimated the pressure associated with the 10^4 K gas on these scales to be

$$p_{\rm nebula} \approx 5.5 \times 10^{-10} \left(\frac{n_e}{200\ {\rm cm}^{-3}}\right) \left(\frac{T}{10^4\ {\rm K}}\right)\ {\rm dyn\ cm}^{-2}. \quad (9)$$

Our estimated central X-ray pressure on the same ∼10-kpc scale is 7×10^{-10} dyn cm^{-2} (Tremblay et al. 2012), very close to what is inferred for the 10^4 K gas, implying that the two phases are in rough pressure equilibrium.

The nebula is associated with a substantial dust component that can be quantitatively studied using the *Herschel* observations. In Fig. 4 we show the radio-through-optical SED of A2597, with the FIR component filled in by the new *Herschel* PACS and SPIRE data (green circles). Following the same method as described in Mittal et al. (2011), a two-temperature blackbody is fitted to the *Herschel* (PACS and SPIRE) and *Spitzer* 24-μm data points to model the contribution by dust to the FIR SED. Our fit assumes a dust absorption coefficient of $\kappa_\nu = 5.6 \times (\nu/3000\,{\rm GHz})^\beta$ m^2 kg^{-1} with a dust emissivity index of $\beta = 2$ (Dunne et al. 2000; Mittal et al. 2011). We note that the 850-μm Submillimetre Common-User Bolometer Array (SCUBA) data point could also be associated with an additional cold dust component, though we choose not to include it in our modelling given the uncertain radio source contribution to this flux.

We find the best-fitting temperature and mass of the warm dust component to be $T_{\rm warm\,dust} = 47 \pm 1.4$ K and $M_{\rm warm\,dust} = (1.7 \pm 0.6) \times 10^5$ M$_\odot$, respectively. The temperature and mass of the cold dust component are found to be $T_{\rm cold\,dust} = 20 \pm 1.7$ K and $M_{\rm cold\,dust} = (1.3 \pm 0.5) \times 10^7$ M$_\odot$, respectively. This two-component blackbody fit could be unrealistic if (1) there is a large population of small dust grains driving a broad emission distribution that might mimic a modified blackbody, and/or (2) if the warm dust grains are heated stochastically (which is only realistic for very small grains; e.g. Draine & Li 2001). Furthermore, a two-temperature fit assumes that there is no dust at temperatures between ∼20 and ∼48 K, which is almost certainly not true. The SPIRE and SCUBA points suggest the presence of very cold dust,

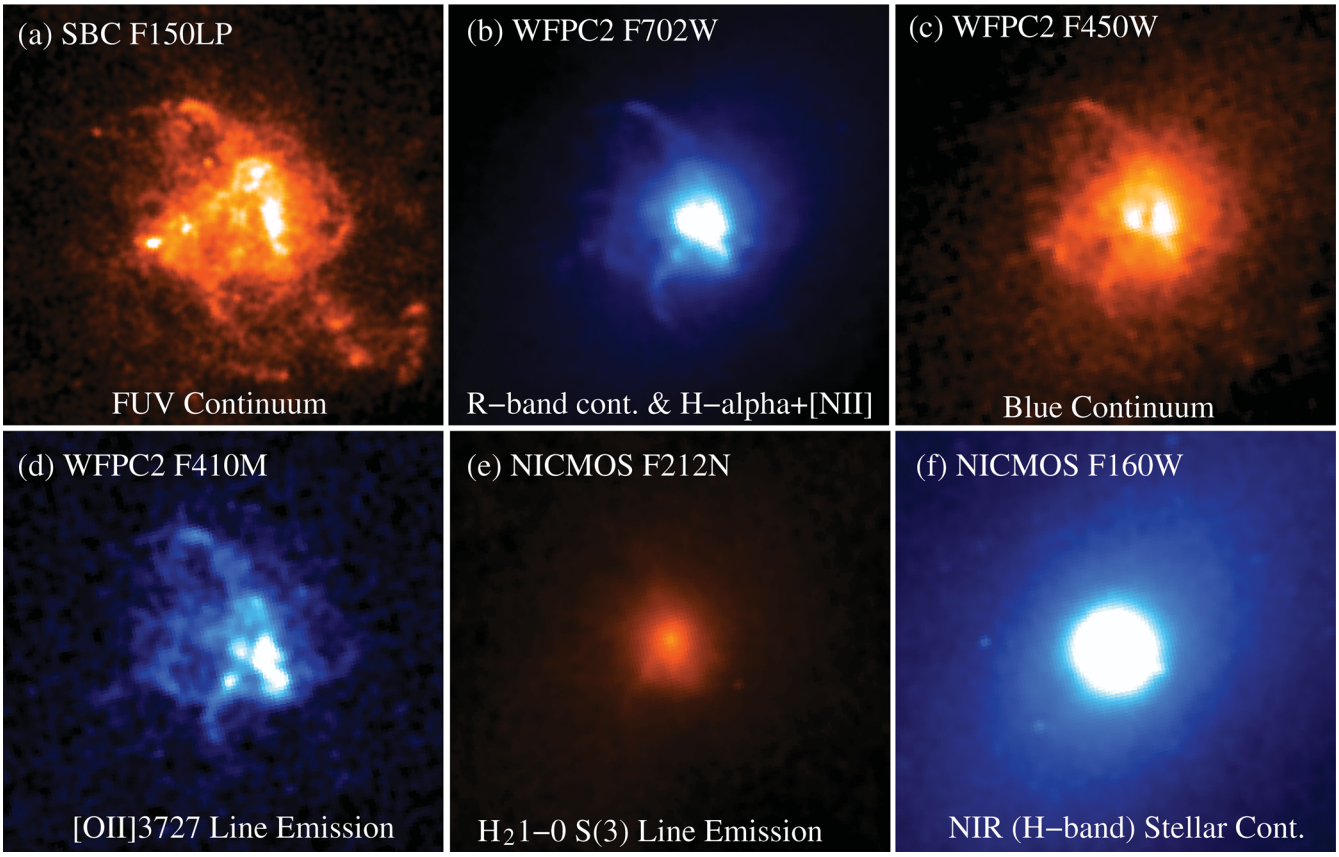

Figure 3. *HST* imaging of FUV, optical, NIR and line emission associated with the ∼10 kpc-scale nebula at the centre of the A2597 BCG. The FOV of each figure is approximately 10×10 arcsec^2 ($\sim 15 \times 15$ kpc^2). Panel (a) is FUV continuum emission, attributed to ongoing star formation, from the ACS Solar Blind Channel (SBC) F150LP observation of Oonk et al. (2011). Lyα emission is not included in the bandpass. Panel (b) is *R*-band optical continuum, Hα+[N II], and [S II] emission from Holtzman et al. (1996). Panel (c), also from Holtzman et al. (1996), contains blue optical continuum and a small contribution from [O II] λ3727 Å emission, which dominates the bandpass in the F410M image shown in panel (d), from Koekemoer et al. (1999). Panel (e) is primarily emission from the 1.956-μm (rest frame) 1−0 *S*(3) H_2 line, originally published by Donahue et al. (2000). Panel (f) is *H*-band NIR stellar continuum emission, also from Donahue et al. (2000).

which would increase the mass limit. Finally, the best-fitting dust mass is extremely sensitive to the assumed dust temperature, which in turn is degenerate with the dust emissivity index β. We have assumed that $\beta = 2$, but the value can vary between ∼1.5 and 2 (e.g. Tabatabaei et al. 2011). While we find that varying β between these values does not significantly change our results, we stress that the dust masses and temperatures listed here are extremely assumption-heavy. Altering these assumptions even slightly can significantly alter the result. As a point of illustration, the single-temperature fit to the A2597 *Herschel* points by Rawle et al. (2012) finds $T = 31$ K and $M_{\rm dust} = 1.6 \times 10^8$ M$_\odot$, an order of magnitude higher than our result. Ultimately, we lack the data to speak affirmatively about the validity of these many assumptions.

With these disclaimers noted, our total *Herschel*-derived dust mass of $M_{\rm cold\,dust} = 1.3 \times 10^7$ M$_\odot$ compared to the inferred molecular gas mass of $1.8 \pm 0.3 \times 10^9$ M$_\odot$ implies a gas-to-dust ratio of $\gtrsim$140. We again stress that, while *Herschel* can place the tightest available constraints on the A2597 dust mass, this gas-to-dust ratio remains an uncertain lower limit given (1) the dust mass, temperature and fit parameter degeneracies discussed above, and (2) CO-inferred molecular gas masses are inherently uncertain because of the CO–H_2 conversion 'X factor' (e.g. Liszt, Pety & Lucas 2010 and references therein). This is especially true considering the apparent low metallicity of the gas, which could mean that our assumed CO–H_2 conversion factor is an order of magnitude too low (e.g. Bolatto et al. 2011). We could therefore be significantly underestimating the gas mass.

Nevertheless, the inferred lower limit ratio is comparable to Galactic ratios, and somewhat low relative to past estimates for other CC BCGs (e.g. Edge 2001). These older ratios suffer from an inability (at the time) to place convincing limits on CC BCG dust masses, so a more comprehensive study with the new *Herschel* sample is needed to better understand the 'typical' gas-to-dust ratios of CC BCGs (assuming such a typical ratio exists – it certainly may not). Unpublished and science demonstration phase results for the *Herschel* CC BCG sample so far indicate more MW-type gas-to-dust ratios on average (e.g. Edge et al. 2010a,b; Rawle et al. 2012; Oonk et al., in preparation).

The *Herschel* [C II]-to-FIR luminosity ratio, which is a tracer of the relative cold gas and dust cooling rates, is ∼0.014 for A2597. This value is high relative to similarly FIR luminous star-forming galaxies (whose [C II]/$L_{\rm FIR}$ ratios are generally an order of magnitude lower). The ratio seems to be higher for lower metallicity galaxies (e.g. Maiolino et al. 2009 and references therein), so the relatively high ratio estimated for A2597 could be partially due to lower metallicity gas, consistent with a cooling flow scenario.

The MW-type gas-to-dust ratio means that the star-forming gas in A2597 is quite dusty. This is inconsistent with a scenario wherein

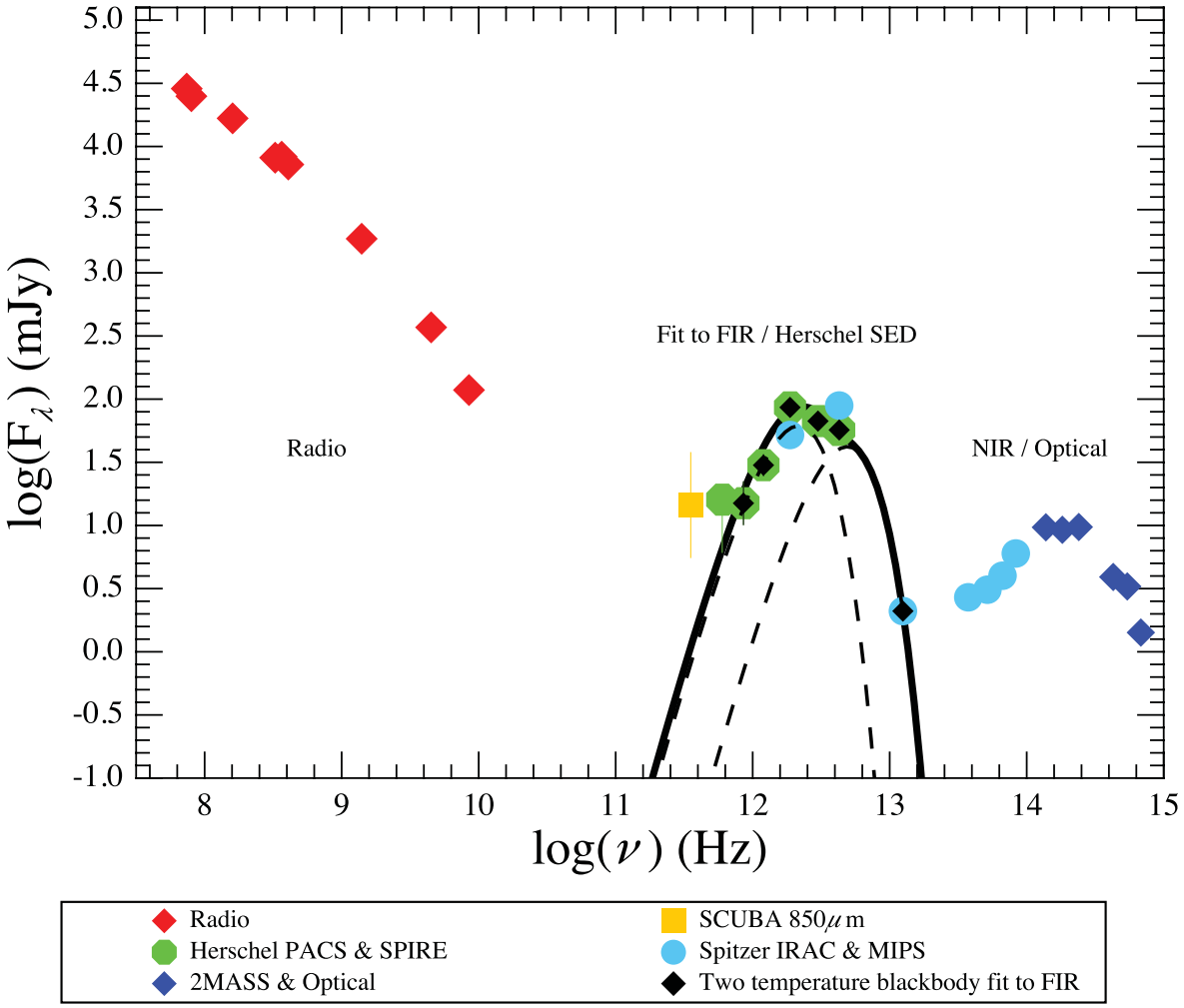

Figure 4. Spectral energy distribution of A2597, from radio (left side) through optical (right side) frequencies. References for the data points used in this plot can be found in Table 1. Following the method from Mittal et al. (2011), a two-temperature blackbody has been fitted to the FIR portion of the SED, sampled by the new *Herschel* PACS and SPIRE observations. See Section 4.3 for a discussion of this figure. The 500-μm SPIRE point is an upper limit. Because the plot is log-log, the error bars on most points are smaller than the points themselves.

already dusty gas originates in the hot atmosphere, where grain sputtering time-scales are short (e.g. Draine & Salpeter 1979, review by Draine 2003). In this case, one might expect far higher gas-to-dust ratios (i.e. dust-poor gas) stemming from cooling flow origin scenarios. Furthermore, even if the cooling flow gas were dusty despite short grain destruction times, then extended FIR emission might be expected on the same scales as the X-ray gas, as dust emission should be a major channel of energy loss for the cooling ICM. This extended FIR emission cannot be detected in A2597 by *Herschel* due to spatial resolution limitations (Edge et al. 2010a,b).

The above result suggests that while the cooling ICM may contribute the bulk of the cold gas in A2597, it cannot contribute the substantial dust component associated with that cold gas. Instead it is more likely that the bulk of the dust component is contributed by stellar mass loss [e.g. via dust-rich asymptotic giant branch (AGB) winds and supernovae]. Modern cooling flow models suggest that cooling from the ICM concentrates in thermally unstable clouds and filaments (e.g. Fabian et al. 2011). In these thermal instabilities, the cooling/cold gas may shield the dust from sputtering. The recent detection by Donahue et al. (2011) of polycyclic aromatic hydrocarbon (PAH) emission in A2597 almost certainly necessitates such a shielding mechanism, given the extreme fragility of PAH molecules in hot ambient environments. If the dust is not efficiently shielded within the filaments, then dust production rates must be higher than what is implied by most models for dust production.

Voit & Donahue (2011) argue that mass loss from the old stellar population of the BCG is indeed a significant source of dusty gas in many CC clusters. We note that this scenario is not at odds with the residual cooling flow model for A2597. As filaments condense from the cooling hot atmosphere, they do so within the stellar body of the galaxy and should therefore contain existing stars within their volume. Voit & Donahue (2011) suggest that the ejected dust-rich envelopes stemming from the old stellar component are not assimilated into the hot phase, but rather remain cold and confined to the cold ambient clouds and filaments, where the dust may be shielded from interaction with the hot phase. If the old stellar component plays an important role in enriching the filaments with dust, then it is likely that it at least plays a non-negligible role in contributing to the observed cold gas mass as well.

5 NEW RESULTS ON STAR FORMATION

5.1 *Herschel* constraints on the star formation rate

The 8−1000 μm luminosity can be used with the Kennicutt relation to estimate the FIR-inferred star formation rate (Kennicutt 1998):

$$\frac{\mathrm{SFR}}{\mathrm{M_\odot\ yr^{-1}}} \lesssim 4.5 \times \left(\frac{L_{\mathrm{FIR}}}{10^{44}\ \mathrm{erg\ s^{-1}}}\right). \quad (10)$$

Using $L_{\mathrm{FIR}} = (6.50 \pm 1.35) \times 10^{43}$ erg s^{-1} ($1.69 \pm 0.35 \times 10^{10}\,\mathrm{L_\odot}$) derived from the *Herschel* data, we find $\mathrm{SFR_{FIR}} \lesssim 2.93 \pm 0.69\,\mathrm{M_\odot\ yr^{-1}}$. This is consistent with the many past SFRs estimated for A2597, which range from 2 to $12\,\mathrm{M_\odot\ yr^{-1}}$ depending on the method used (McNamara & O'Connell 1993; O'Dea et al. 2004; Donahue et al. 2007; Oonk et al. 2011; Rawle et al. 2012). Estimates of star formation rates (particularly in the FUV) are extremely sensitive to internal extinction by dust. The Balmer sequence in A2597 suggests that the internal extinction is significant (about one magnitude in the V band, i.e. $A_V \sim 1$; Voit & Donahue 1997; Oonk et al. 2011), consistent with the substantial dust mass inferred from the *Herschel* data.

5.2 Star formation entropy threshold

Using numerical simulations and ignoring thermal conduction, Sharma et al. (2011) showed that local thermal instabilities in a cooling flow will only produce a multiphase, star-forming ISM when the ratio of the thermal instability time-scale t_{TI} to the local gravitational free-fall time-scale t_{ff} is $t_{\mathrm{TI}}/t_{\mathrm{ff}} \lesssim 10$ (see Sharma et al. 2011 for definitions of these quantities). Expressed in terms of the gas entropy S, this thermal instability threshold is $S \sim 20\,\mathrm{keV\ cm^2}$. Importantly, this theoretical result is very close to the observed $S \sim 30\,\mathrm{keV\ cm^2}$ star formation onset threshold discussed by Rafferty et al. (2008) and Cavagnolo et al. (2008).

The $t_{\mathrm{TI}}/t_{\mathrm{ff}} \lesssim 10$ threshold is marked in the green line on the X-ray cooling time profile in Fig. 5 (left-hand panel) as well as in Fig. 5 (right-hand panel), in which we plot the $t_{\mathrm{TI}}/t_{\mathrm{ff}}$ ratio versus cluster-centric radius. In both panels, we mark maximal radial extent of (a) Lyα, FUV continuum associated with star formation, as well as warm and cold molecular gas inferred from VLT, *HST*, CO and *Herschel* observations and (b) the X-ray cavity network with blue and red shaded regions, respectively. Note that the X-ray cavity network (red region) overlaps with the blue region, meaning it also extends inwards to the cluster centre (as can be seen in the bottom two panels of Fig. 1). We calculate the $t_{\mathrm{TI}}/t_{\mathrm{ff}}$ ratio from the X-ray data by fitting third-order polynomials in log space to the temperature and pressure profiles, then analytically differentiating the logarithmic pressure profile to obtain the free-fall time. We account for the presence of the BCG by setting a minimum value for the gravitational acceleration g to be that of a singular isothermal sphere with a velocity dispersion of 250 km s^{-1}. This BCG contribution is only important at radii $\lesssim$10 kpc.

As discussed in Sharma et al. (2011), the thermal instability time-scale can be approximated as a multiple of the cooling time that is dependent upon how much AGN heating one includes in the model. While the curve in Fig. 5 (right-hand panel) is for pure free–free cooling, including a heating component could scale it upwards by a factor of ∼2 (for moderate heating) to ∼3 (for strong heating). Regardless of whether or not heating is included, the Sharma et al. (2011) predictions are roughly consistent with observations in the case of A2597. The same is true of the $30\,\mathrm{keV\ cm^{-2}}$ star formation entropy threshold discussed by Rafferty et al. (2008) and Cavagnolo et al. (2008) – we do not mark this threshold, but it would lie in nearly the same locations as the green lines in both panels of Fig. 5. Therefore, in either case, the threshold lies just outside the region containing star formation, ionized and molecular gas, and X-ray cavities.

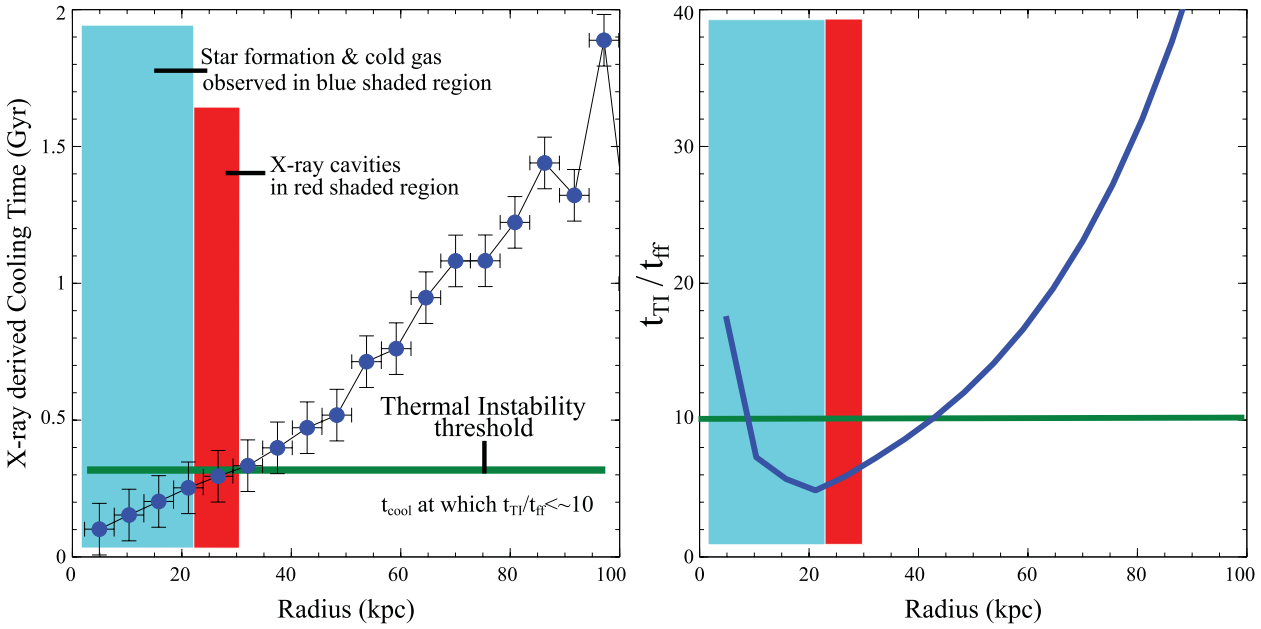

Figure 5. Left panel: X-ray cooling time profile versus cluster-centric radius. The green line marks the $t_{\mathrm{TI}}/t_{\mathrm{ff}} \lesssim 10$ thermal instability threshold discussed by Sharma et al. (2011), where t_{TI} is the thermal instability time-scale and t_{ff} is the local gravitational free-fall time-scale. Sharma et al. (2011) suggest that, beyond this threshold, a cooling flow can form thermally unstable, star-forming clouds and filaments. The blue shaded region marks the largest radial extent of observed ionized and molecular gas. The red shaded region, which overlaps it, marks the largest radial extent at which X-ray cavities are observed. Right panel: ratio of the thermal instability time-scale and free-fall time-scales versus cluster-centric radius. The same $t_{\mathrm{TI}}/t_{\mathrm{ff}} \lesssim 10$ star formation threshold is marked with a green line. See Section 5.2 for a discussion of these profiles.

This apparent threshold would be difficult to understand if the cold gas fuelling star formation was supplied by a merger. One might imagine such a scenario if there were a steep radial gradient in thermal conduction efficiency, such that clouds introduced by a merger no longer evaporate at the radius where conduction no longer outpaces radiative cooling. This is purely speculative, however, and the results presented here strongly suggest that a residual cooling flow from the ambient hot atmosphere is the primary contributor of the warm and cold gas in A2597. We provide further supporting evidence for this suggestion in the following section.

5.3 Evidence for filamentary cooling channels

In the top left panel of Fig. 6 we show the extended filamentary Lyα emission (*HST*/STIS, from O'Dea et al. 2004), whose brightness can be accounted for by photoionization from the underlying FUV continuum emission stemming from the young stellar component, shown in the top right panel of Fig. 6 (*HST*/ACS, from Oonk et al. 2010). In the top left panel, we show the adaptively smoothed 0.5–7 keV X-ray contours in green (with the central contours removed to aid viewing), and the 330-MHz, 1.3-GHz and 8.4-GHz radio contours in black, blue and white, respectively. In the top right panel we use red contours to mark the outermost boundary at which low surface brightness FUV continuum emission is observed at a level of 2σ above the background.

The faint underlying FUV continuum follows the extended bright Lyα clumps and filaments northwards and southwards, out to a cluster-centric radius of nearly 20 kpc. In the X-ray temperature map presented in Tremblay et al. (2012), there is an elongated region of cold X-ray gas extending along the same N–S projected axis. This filamentary axis is also significantly offset in position angle from the cavity/radio 'AGN heating axis'. The north-eastern Lyα filaments lie along a rim bordering the cold X-ray filament (feature 5 in Fig. 1), which could be due to the star-forming gas having been swept outwards by the 1.3-GHz radio source (or by the soft X-ray filament that the radio source may have dredged upwards; e.g. Tremblay et al. 2012).

In the bottom two panels of Fig. 6 we show the 0.5–7 keV unsmoothed X-ray data, with an aggressive colour scale stretch applied to enhance the contrast. Lyα contours are overlaid on the bottom left panel. Note how the northern bright X-ray knot bends 5 kpc upwards to follow the high surface brightness Lyα and FUV continuum emission. The red boxes in the bottom right panel of Fig. 6 mark the sectors from which we extract and model X-ray spectral data. These sectors approximately cover the region over which the extended Lyα and FUV continuum filaments are cospatial with the soft X-ray gas. As stated previously, this is also the axis along which elongated cooler X-ray gas is observed in the X-ray temperature map. Following the method described by Tremblay et al. (2012), a cooling flow model (WABS$\times$MKCFLOW) fit to the spectra extracted from these sectors finds a combined mass deposition rate of $\sim 7 \pm 0.5\,\mathrm{M}_{\odot}\,\mathrm{yr}^{-1}$ associated with the region of X-ray gas cospatial with the ionized filaments. This is roughly comparable to the local star formation rate estimated from FUV emission in the filaments. A multicomponent fit to the X-ray spectral data (e.g. Sanders et al. 2004) suggests that multiphase gas could be present, though the quality of the fits prevents any conclusions from being made. That these regions could account for a significant fraction of the residual cooling luminosity is consistent with recent similar results on Perseus and Abell 2146 from Fabian et al. (2011) and Russell et al. (2012), respectively.

This result serves as further supporting evidence to our overall suggestion that (a) ICM cooling contributes a significant fraction of the cold gas budget fuelling the star formation and (b) this cooling happens in a spatially discrete, structured manner concentrated in filaments. In the case of A2597, these filaments may preferentially be found in a cooling channel that is nearly perpendicular to the projected AGN heating axis permeated by X-ray cavities and radio emission. Future Atacama Large Millimeter/submillimeter Array (ALMA) observations capable of spatially resolving molecular gas emission on the scale of the filaments will be necessary to either refute or reinforce the above claims.

5.4 Evidence for both triggered and persistent star formation amid AGN feedback

The frequently studied morphological correspondence of blue excess filaments with the 8.4-GHz radio source in A2597 presents an important test case for models of jet-induced star formation. The morphological evidence can be seen in the left panel of Fig. 7, in which we show an unsharp mask of the FUV continuum emission. The leading edge of the northern 8.4-GHz radio lobe, shown in red contours, spatially correlates with the northernmost FUV arc, which might be expected if star formation is triggered by shock-induced cloud collapse as the propagating plasma entrains and displaces cold gas phases (see e.g. the shock-/jet-induced star formation models by Elmegreen & Elmegreen 1978; Voit 1988; De Young 1989; McNamara & O'Connell 1993).

The optical integral field unit (IFU) spectroscopy of Oonk et al. (2010) may lend evidence in support of this, as it shows high-velocity dispersion molecular gas along the 'sweep-up' trajectory leading to the northern FUV arc. Further evidence for gas displacement by (or perhaps dynamical confinement of) the radio source can be seen in the southern lobe, which anticorrelates with the local FUV distribution. It is also worth noting that the 'U'-shaped loop of filamentary star formation directly southwest of the southern radio lobe is extended along the general axis of the 330-MHz radio source and the large western X-ray cavity. The compelling morphological correspondence has motivated several past investigations of jet-triggered star formation in A2597 (De Young 1995; Koekemoer et al. 1999; O'Dea et al. 2004). Each of these works found the model energetically feasible on time-scales that make sense in relation to the radio source (De Young 1995).

It is worth pursuing these time-scale estimates further, by comparing the estimated radio source and X-ray cavity age limits with the young stellar component dating presented by Oonk et al. (2011), using data from *HST* and the VLT FORS imager. That work compared measured *FUV*/*U*-band ratios with those predicted from Bruzual & Charlot (2003) simple stellar population models. We show the young stellar population (YSP) ages inferred by Oonk et al. (2011) in the right panel of Fig. 7. Note that these estimated ages are better considered in the relative rather than absolute sense. The ages are unavoidably uncertain given the age–metallicity–extinction degeneracy associated with measuring ages of a young stellar component. The *FUV*/*U*-band colour is strongly dependent upon the nature and patchiness of the intrinsic reddening, which cannot be quantified on these scales. Furthermore, while C IV λ1549 Å resonant line emission has so far not been convincingly detected in A2597 (O'Dea et al. 2004; Oonk et al. 2011), a significant contribution from this line would result in an underestimation of stellar ages from the *FUV*/*U*-band colour. We note that C IV has recently been detected in the *HST* Cosmic Origins Spectrograph (COS) FUV spectroscopy of M87 (Sparks et al. 2012).

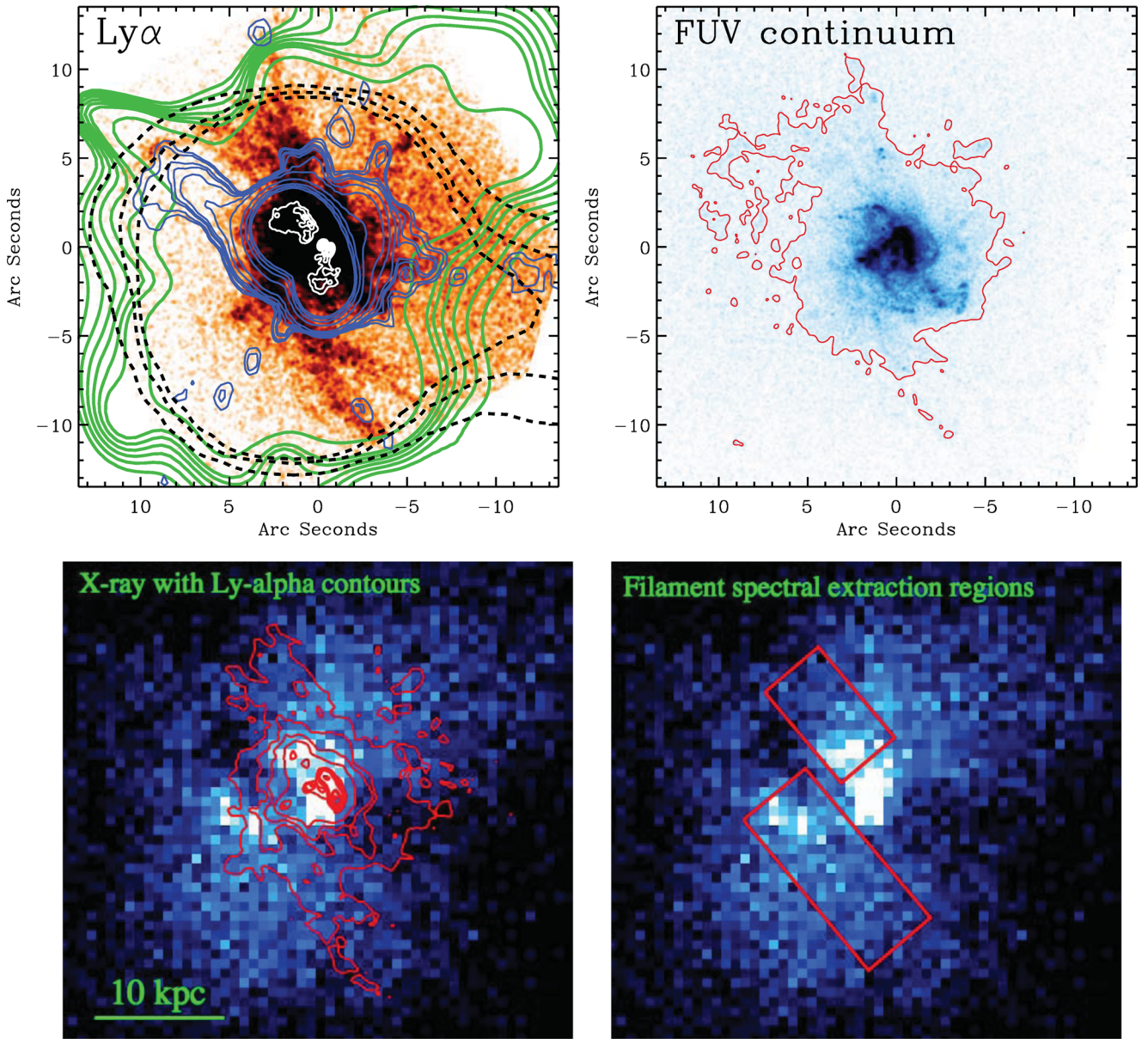

Figure 6. Top left: in red/orange we show the *HST*/STIS FUV observation of extended Lyα emission associated with the A2597 BCG, from O'Dea et al. (2004). 1.3-GHz, 8.4-GHz and 330-MHz radio contours are overlaid in blue, white and black (dashed), respectively, while adaptively smoothed 0.5–7 keV X-ray contours are overlaid in green. We have removed the innermost 1.3-GHz, 330-MHz and X-ray contours to aid viewing. Top right: *HST*/ACS SBC F150LP ∼8-ks exposure of FUV continuum emission associated with the A2597 emission-line nebula. In red contours, we outline the boundary within which low surface brightness FUV continuum emission has been detected at $\sim 2\sigma$ above the background. Bottom left: the unsmoothed 150-ks 0.5–7 keV X-ray data, shown with an aggressive colour scale stretch used to highlight the high surface brightness knots observed near the X-ray centroid. Lyα contours are overlaid in red. The northern high surface brightness X-ray knot bends upwards to follow the overall distribution of the high surface brightness Lyα and FUV continuum emission. Bottom right: the same X-ray image, with red boxes marking the sectors from which X-ray spectral data were extracted and modelled. A WABS×MKCFLOW fit to the data finds a combined mass deposition rate of $\sim 7 \pm 0.5\,\mathrm{M}_{\odot}\ \mathrm{yr}^{-1}$ associated with the X-ray filaments. This is comparable to the local star formation rate estimated from FUV emission in the filaments.

With these caveats in mind, the age map shows younger stars nearer to the radio source. Looking on smaller scales, there is possible evidence of even younger (5 Myr) stars found (a) at the northern edge of the northern radio lobe (where jet-triggered star formation could have recently occurred), and (b) along the projected axis of the host galaxy stellar isophotes. When we compare X-ray cavity ages from this paper with these YSP ages, we find that the range of young stellar ages entirely encompasses the inferred age range of the X-ray cavity network. Oonk et al. (2011) found ages for the YSP ranging from 5 to 700 Myr old, while our estimates for the X-ray cavity ages range from 10 to 200 Myr. The stellar ages also encompass the age range estimated for the radio sources (see Section 3.4). The stellar ages inferred by Oonk et al. (2011) are consistent with similar estimates by Koekemoer et al. (1999).

Two independent studies infer a young star age range with limits that are older and younger than the age limits for the X-ray cavity network. While acknowledging the many caveats associated with these estimates, this could imply that low levels of star

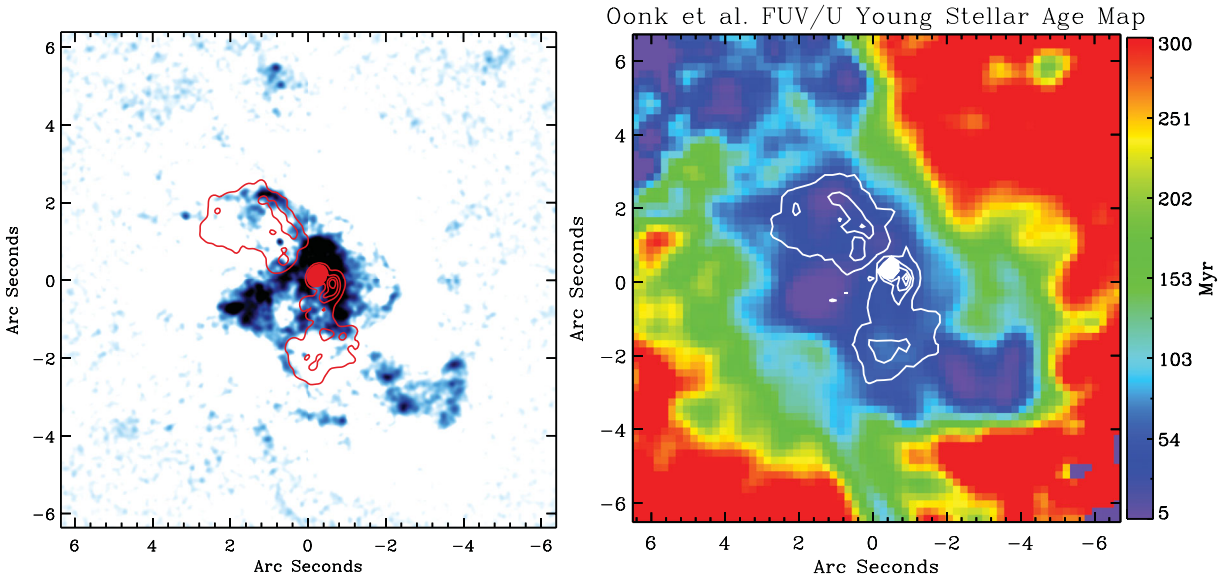

Figure 7. Left panel: unsharp mask of the 8-ks *HST*/ACS FUV continuum image shown in Fig. 6. Note the strong spatial correspondence of the northern arc of FUV emission with the leading edge of the 8.4-GHz radio lobe, which is outlined in red contours. There is also evidence that the southern radio lobe has swept out the star-forming gas, or has been allowed to expand after emerging from the dense gaseous medium. Right panel: single stellar population (SSP) age map from Oonk et al. (2011), made by comparing observed FUV/*U*-band ratios (from *HST* and the VLT, respectively) to those predicted from Bruzual & Charlot (2003) models. The youngest portion of the young stellar component is found nearer to the central 8.4-GHz radio source, which we overlay in white contours. The young stars also extend northwards along the region threaded by Lyα and FUV continuum filaments (as can be seen by comparing this figure with Fig. 6).

formation (2–12 $M_\odot$ yr^{-1}) have managed to persist even amid the AGN feedback-driven excavation of the X-ray cavities. The stellar age spatial distribution may further suggest that star formation was more spatially extended in the past. This interpretation is ambiguously dependent upon the likely fact that most star formation occurs in the filaments, which are more concentrated in the centre than in the periphery. Nevertheless, we cannot rule out the possibility that even if the star formation has been persistent during the current AGN feedback episode, it may be qualitatively changing with time (i.e. declining and becoming more spatially concentrated).

6 CONCLUDING DISCUSSION

The results presented in this paper, considered in the context of three decades of previous work on A2597, motivate the following general conclusion: while radio-mode AGN feedback has injected enough energy into the hot ICM to inhibit the classical cooling flow, the source harbours a residual cooling flow at 4–8 per cent of the expected classical rates, giving rise to star formation amid the $\sim 10^9$ $M_\odot$ cold molecular gas reservoir in the nucleus. While we cannot rule out cold gas contributions from mergers or tidal stripping, we suggest that the cooling ICM is likely the dominant supply channel for cold gas to the nucleus in A2597.

A simple test of this model can be made by considering the predicted residual cooling flow mass deposition rate with the observed mass of the cold molecular gas reservoir, along with the star formation and black hole accretion rates. Together, these can be considered the ultimate mass sinks of the residual cooling flow, so their mass and energy budgets should be consistent with one another. In Table 3 we compile the various mass, mass flux, energy and time-scale limits assembled throughout the course of this analysis. We separate out the important quantities related to inhibition of the classical cooling flow (i.e. the classical mass deposition rate and the lower limit kinetic energy input estimate based on X-ray cavity analysis). We then list the multiphase constraints on the residual cooling flow model. The predicted residual mass deposition rates are roughly 20−40 $M_\odot$ yr^{-1} within 30 kpc. A steady residual mass deposition rate of this magnitude would accumulate the observed $\sim 10^9$ $M_\odot$ of gas in the central 30 kpc within $\lesssim 10^8$ yr. Taking the ratio of the observed molecular gas mass to the observed star formation rate yields a gas depletion time-scale that is also of the order of 10^8 years. It is therefore possible for there to be an approximately steady-state distribution of multiphase gas masses over the AGN lifetime, with a possible slow accumulation of cold gas at a rate comparable to the difference between the local mass deposition and star formation rates.

While the proposed model appears successful in this regard, the above argument is of course very qualitative. Gaspari et al. (2012) presented a follow-up study to the Sharma et al. (2011) results, predicting (among other things) the mass budgets expected from various cooling flow recipes, over time, in the innermost 20 kpc of a BCG. Their results for an uninhibited cooling flow expectedly overpredict the mass of the warm and cold phases by several orders of magnitude. When they include AGN heating at varying efficiencies, their results fall more in line – albeit on the high end – with what is observed in A2597. Their feedback-inhibited residual cooling flow models predict a roughly steady accretion rate of $\sim 10\,M_\odot$ yr^{-1} of $T < 5 \times 10^5$ K gas within the central 20 kpc. After 1 Gyr, this accretion rate would accumulate a $\sim 5 \times 10^{10}$ $M_\odot$ cold gas reservoir, which is an order of magnitude more massive than what has been measured in A2597. However, as Gaspari et al. (2012) note, their simulations do not include star formation, which could reduce the accumulation rate of cold gas by an order of magnitude. On roughly the same scale, the highest measured SFR for A2597 is $\sim 10\,M_\odot$ yr^{-1}, which is roughly the cold gas accretion rate predicted on the same scale by Gaspari et al. (2012). It is also similar to the X-ray-derived mass deposition rate for the region cospatial with the filaments of ionized gas, as discussed in Section 5.3.

Table 3. A summary of the various mass, mass flux, energy and time-scale limits compiled as part of this paper. All values are measured or estimated at or within a central radius of 30 kpc. Column (1): temperature range of the ISM phase (if applicable); column (2): qualitative description of that phase or feature; column (3): mass associated with the phase or feature; column (4): power associated with the phase or feature; column (5): estimated mass conversion flux or deposition rate; column (6): a rough time-scale associated with the listed phase or feature. $t_{\rm cool}$ is a cooling time associated with the listed cooling flow. $t_{\rm heat}$ is a crude estimate of the possible time-scale over which X-ray cavity enthalpy could be dissipated as heat in the ISM, limited by the cavity lifetime. $t_{\rm deplete}$ is the cold gas depletion time-scale, set by the ratio of the observed cold molecular gas mass and the star formation rate. $t_{\rm accum}$ is the time it would take the predicted residual cooling flow mass deposition rate to accumulate the observed cold molecular gas mass. Note that the corresponding time-scales ($t_{\rm cool}$ versus $t_{\rm heat}$ and $t_{\rm accum}$ versus $t_{\rm deplete}$) roughly balance one another.

ISM Phase (K) (1)	Feature (2)	$M_{\rm phase}(R \lesssim 30\,{\rm kpc})$ ($M_\odot$) (3)	$L(R \lesssim 30\,{\rm kpc})$ (erg s^{-1}) (4)	$\dot{M}\left(R \lesssim 30\,{\rm kpc}\right)$ ($M_\odot$ yr^{-1}) (5)	t ($\times 10^7$ yr) (6)
		Limits on a classical cooling flow			
10^7-10^8	Classical cooling flow	···	$(1-4)\times10^{44}$	$\dot{M}_{\rm cool} \sim 100-500$	$t_{\rm cool} \sim 30$
···	AGN feedback input	···	$>1.89\times10^{44}$	···	$t_{\rm heat} \sim 1-40$
		Limits on a residual cooling flow			
10^7-10^8	Residual cooling flow	···	$(0.4-3.2)\times10^{43}$	$\dot{M}_{\rm cool} \sim 20-40$	$t_{\rm accum} \sim 10$
10^6	FUV cooling flow	···	$\gtrsim 4\times10^{40}$	$\dot{M}_{\rm cool} \lesssim 40$	···
10^4-10^5	Warm ionized gas	$\gtrsim 9.7\pm0.3\times10^6$	$\gtrsim 3.5\times10^{41}$	$\dot{M}_{\rm SFR} \sim 2-12$	···
$10-10^3$	Warm/cold molecular gas	$\gtrsim 1.8\pm0.3\times10^9$	$\gtrsim 5\times10^{41}$	···	$t_{\rm deplete} \sim 10$

7 SUMMARY

We have presented a multiwavelength study of the central brightest cluster galaxy in the CC cluster A2597. The main results of this paper can be summarized as follows.

(i) New *Chandra* observations reveal the X-ray cavity network to be more extensive than previously known, and associated with enough enthalpy to locally inhibit the classical cooling flow.

(ii) A comparison of estimated cavity and radio source ages suggests that the AGN duty cycle is near to 100 per cent, requiring a near-steady sub-Eddington flow of gas to the nucleus.

(iii) The *Herschel*-derived warm dust temperature and mass is estimated to be $T_{\rm warm\,dust} = 47 \pm 1.4$ K and $M_{\rm warm\,dust} = (1.7 \pm 0.6)\times10^5\,M_\odot$, respectively. The temperature and mass of the cold dust component is found to be $T_{\rm cold\,dust} = 20 \pm 1.7$ K and $M_{\rm cold\,dust} = (1.3 \pm 0.5)\times10^7\,M_\odot$, respectively. We discuss important uncertainties and assumptions associated with these values in Section 4.3.

(iv) We present an updated CO-inferred cold molecular gas mass of $(1.8 \pm 0.3)\times10^9\,M_\odot$, using previously unpublished CO(2−1) IRAM 30-m observations.

(v) The newly measured gas and dust masses yield a relatively low, Galactic-type gas-to-dust ratio of $\gtrsim$140, so the gas is dusty. We argue that mass loss from evolved stars is the most likely source of this substantial dust component. A shielding mechanism is likely required to protect the grains from interaction with the ambient hot ISM.

(vi) The warm and cold gas phases are approximately cospatial with the coolest regions of X-ray gas.

(vii) Dynamical constraints on the central cold gas component do not permit large-scale rotation or major asymmetric velocity structures, consistent with a scenario wherein the cold gas is accreted with low net angular momentum, inconsistent with what is expected from a merger.

(viii) The theoretical thermal instability threshold lies just outside the observed $\lesssim$30 kpc X-ray cavity network. Molecular and ionized, star-forming gas lies interior to both. This result is consistent with theoretical predictions of the entropy threshold at which ICM cooling begins to form thermally unstable cold clouds and filaments.

(ix) X-ray-derived mass deposition rates along regions cospatial with star-forming filaments are consistent with the locally estimated star formation rates, strongly suggesting a causal connection.

(x) The young stellar component occupies an age range that is apparently wider than that for the X-ray cavities. This could suggest that star formation has persisted amid the feedback-driven excavation of the X-ray cavity network. Localized sites of star formation may also have been triggered by the propagating radio source.

We conclude that a residual cooling flow with a strength of 4–8 per cent of the expected classical mass deposition rates is the dominant contributor of the cold gas reservoir fuelling star formation and AGN activity in the A2597 BCG.

ACKNOWLEDGMENTS

The authors thank Drs Elaine Sadler, Robert Laing, Andy Robinson, Joel Kastner and Bill Sparks for thoughtful discussions. We also thank the anonymous referee for constructive feedback. GRT is grateful to Ruth Smith, and acknowledges support from the NASA/NY Space Grant Consortium, as well as a European Southern Observatory (ESO) Fellowship partially funded by the European Community's Seventh Framework Programme (/FP7/2007-2013/) under grant agreement No. 229517. Partial support was provided by NASA through an award issued by JPL/Caltech, as well as the Radcliffe Institute for Advanced Study at Harvard University. TEC was partially supported by NASA through *Chandra* award G06-7115B issued by the *Chandra* X-ray Observatory Center for and on behalf of NASA under contract NAS8-39073. Basic research into radio astronomy at the Naval Research Laboratory is supported by 6.1 Base funds. CLS was supported in part by NASA *Herschel* Grants RSA 1373266, RSA P12-78175 and *Chandra* Grant G01-12169X. ACF thanks the Royal Society. This paper is based upon observations with the *Chandra X-ray Observatory*, which is operated by the Smithsonian Astrophysical Observatory for and on behalf of NASA under contract NAS8-03060. We also present observations made with the *Herschel Space Observatory*, a European

Space Agency Cornerstone Mission with significant participation by NASA. We make use of previously published observations by the NASA/ESA *Hubble Space Telescope*, obtained at the Space Telescope Science Institute, which is operated by the Association of Universities for Research in Astronomy Inc., under NASA contract 5-26555. The National Radio Astronomy Observatory is a facility of the National Science Foundation operated under cooperative agreement by Associated Universities Inc. We have made extensive use of the NASA Astrophysics Data System bibliographic services and the NASA/IPAC Extragalactic Database, operated by the Jet Propulsion Laboratory, California Institute of Technology, under contract with NASA.

REFERENCES

Abell G. O., 1958, ApJS, 3, 211
Abell G. O., Corwin H. G., Jr, Olowin R. P., 1989, ApJS, 70, 1
Allen R. J., 1969, A&A, 3, 382
Allen S. W., 1995, MNRAS, 276, 947
Allen S. W., Fabian A. C., Johnstone R. M., Arnaud K. A., Nulsen P. E. J., 2001, MNRAS, 322, 589
Baan W. A., Haschick A. D., Burke B. F., 1978, ApJ, 225, 339
Batcheldor D., Tadhunter C., Holt J., Morganti R., O'Dea C. P., Axon D. J., Koekemoer A., 2007, ApJ, 661, 70
Baum S. A., 1987, PhD thesis, Maryland Univ.
Baum S. A., O'Dea C. P., 1991, MNRAS, 250, 737
Begelman M. C., 2001, ApJ, 551, 897
Best P. N., Kauffmann G., Heckman T. M., Ivezić Ž., 2005, MNRAS, 362, 9
Best P. N., von der Linden A., Kauffmann G., Heckman T. M., Kaiser C. R., 2007, MNRAS, 379, 894
Bildfell C., Hoekstra H., Babul A., Mahdavi A., 2008, MNRAS, 389, 1637
Bîrzan L., Rafferty D. A., McNamara B. R., Wise M. W., Nulsen P. E. J., 2004, ApJ, 607, 800
Blanton E. L., Sarazin C. L., McNamara B. R., Wise M. W., 2001, ApJ, 558, L15
Blanton E. L., Randall S. W., Clarke T. E., Sarazin C. L., McNamara B. R., Douglass E. M., McDonald M., 2011, ApJ, 737, 99
Böhringer H., Voges W., Fabian A. C., Edge A. C., Neumann D. M., 1993, MNRAS, 264, L25
Bolatto A. D. et al., 2011, ApJ, 741, 12
Bregman J. N., Lloyd-Davies E. J., 2006, ApJ, 644, 167
Brighenti F., Mathews W. G., 2003, ApJ, 587, 580
Bruzual G., Charlot S., 2003, MNRAS, 344, 1000
Burns J. O., 1990, AJ, 99, 14
Cardiel N., Gorgas J., Aragón-Salamanca A., 1998, Ap&SS, 263, 83
Cavagnolo K. W., Donahue M., Voit G. M., Sun M., 2008, ApJ, 683, L107
Churazov E., Brüggen M., Kaiser C. R., Böhringer H., Forman W., 2001, ApJ, 554, 261
Churazov E., Sunyaev R., Forman W., Böhringer H., 2002, MNRAS, 332, 729
Clarke T. E., Sarazin C. L., Blanton E. L., Neumann D. M., Kassim N. E., 2005, ApJ, 625, 748 (C05)
Conselice C. J., Gallagher J. S., III, Wyse R. F. G., 2001, AJ, 122, 2281
Crawford C. S., Fabian A. C., 1993, MNRAS, 265, 431
Crawford C. S., Fabian A. C., Johnstone R. M., Arnaud K. A., 1989, MNRAS, 236, 277
De Young D. S., 1989, ApJ, 342, L59
De Young D. S., 1995, ApJ, 446, 521
De Young D. S., Roberts M. S., 1974, ApJ, 189, 1
Donahue M., Voit G. M., 1991, ApJ, 381, 361
Donahue M., Mack J., Voit G. M., Sparks W., Elston R., Maloney P. R., 2000, ApJ, 545, 670
Donahue M. et al., 2007, ApJ, 670, 231
Donahue M., de Messières G. E., O'Connell R. W., Voit G. M., Hoffer A., McNamara B. R., Nulsen P. E. J., 2011, ApJ, 732, 40
Draine B. T., 2003, ARA&A, 41, 241
Draine B. T., Li A., 2001, ApJ, 551, 807
Draine B. T., Salpeter E. E., 1979, ApJ, 231, 77
Dunn R. J. H., Fabian A. C., 2006, MNRAS, 373, 959
Dunne L., Eales S., Edmunds M., Ivison R., Alexander P., Clements D. L., 2000, MNRAS, 315, 115
Dursi L. J., Pfrommer C., 2008, ApJ, 677, 993
Edge A. C., 2001, MNRAS, 328, 762
Edge A. C., Frayer D. T., 2003, ApJ, 594, L13
Edge A. C., Wilman R. J., Johnstone R. M., Crawford C. S., Fabian A. C., Allen S. W., 2002, MNRAS, 337, 49
Edge A. C. et al., 2010a, A&A, 518, L47
Edge A. C. et al., 2010b, A&A, 518, L46
Edwards L. O. V., Hudson M. J., Balogh M. L., Smith R. J., 2007, MNRAS, 379, 100
Egami E. et al., 2006, ApJ, 647, 922
El-Zant A. A., Kim W.-T., Kamionkowski M., 2004, MNRAS, 354, 169
Elmegreen B. G., Elmegreen D. M., 1978, ApJ, 220, 1051
Fabian A. C., 1994, ARA&A, 32, 277
Fabian A. C., 2003, MNRAS, 344, L27
Fabian A. C., 2012, ARA&A, in press (arXiv:1204.4114)
Fabian A. C. et al., 2000, MNRAS, 318, L65
Fabian A. C., Celotti A., Blundell K. M., Kassim N. E., Perley R. A., 2002, MNRAS, 331, 369
Fabian A. C., Sanders J. S., Taylor G. B., Allen S. W., Crawford C. S., Johnstone R. M., Iwasawa K., 2006, MNRAS, 366, 417
Fabian A. C., Johnstone R. M., Sanders J. S., Conselice C. J., Crawford C. S., Gallagher J. S., III, Zweibel E., 2008, Nat, 454, 968
Fabian A. C., Sanders J. S., Williams R. J. R., Lazarian A., Ferland G. J., Johnstone R. M., 2011, MNRAS, 417, 172
Fanaroff B. L., Riley J. M., 1974, MNRAS, 167, 31P
Ferland G. J., Fabian A. C., Hatch N. A., Johnstone R. M., Porter R. L., van Hoof P. A. M., Williams R. J. R., 2008, MNRAS, 386, L72
Ferland G. J., Fabian A. C., Hatch N. A., Johnstone R. M., Porter R. L., van Hoof P. A. M., Williams R. J. R., 2009, MNRAS, 392, 1475
Ferrarese L., Merritt D., 2000, ApJ, 539, L9
Forman W. et al., 2005, ApJ, 635, 894
Forman W. et al., 2007, ApJ, 665, 1057
Gaspari M., Ruszkowski M., Sharma P., 2012, ApJ, 746, 94
Gebhardt K. et al., 2000, ApJ, 539, L13
Gitti M., Nulsen P. E. J., David L. P., McNamara B. R., Wise M. W., 2011, ApJ, 732, 13
Griffith M. R., Wright A. E., 1994, VizieR Online Data Catalog, 8027, 0
Hansen L., Jorgensen H. E., Norgaard-Nielsen H. U., 1995, A&A, 297, 13
Hatch N. A., Crawford C. S., Johnstone R. M., Fabian A. C., 2006, MNRAS, 367, 433
Haynes M. P., Brown R. L., Roberts M. S., 1978, ApJ, 221, 414
Heckman T. M., Baum S. A., van Breugel W. J. M., McCarthy P., 1989, ApJ, 338, 48
Hicks A. K., Mushotzky R., 2005, ApJ, 635, L9
Holt J., Tadhunter C. N., Morganti R., 2008, MNRAS, 387, 639
Holt J., Tadhunter C. N., Morganti R., Emonts B. H. C., 2011, MNRAS, 410, 1527
Holtzman J. A. et al., 1996, AJ, 112, 416
Hu E. M., 1992, ApJ, 391, 608
Hu E. M., Cowie L. L., Wang Z., 1985, ApJS, 59, 447
Hudson D. S., Mittal R., Reiprich T. H., Nulsen P. E. J., Andernach H., Sarazin C. L., 2010, A&A, 513, A37
Hutchings J. B., Balogh M. L., 2000, AJ, 119, 1123
Jaffe W., Bremer M. N., 1997, MNRAS, 284, L1
Jaffe W., Bremer M. N., van der Werf P. P., 2001, MNRAS, 324, 443
Jaffe W., Bremer M. N., Baker K., 2005, MNRAS, 360, 748
Johnstone R. M., Fabian A. C., Nulsen P. E. J., 1987, MNRAS, 224, 75
Johnstone R. M. et al., 2012, MNRAS, submitted
Kaufman M. J., Wolfire M. G., Hollenbach D. J., Luhman M. L., 1999, ApJ, 527, 795
Kennicutt R. C., Jr, 1998, ApJ, 498, 541

Koekemoer A. M., O'Dea C. P., Sarazin C. L., McNamara B. R., Donahue M., Voit G. M., Baum S. A., Gallimore J. F., 1999, ApJ, 525, 621
Lim J., Ohyama Y., Chi-Hung Y., Dinh-V-Trung, Shiang-Yu W., 2012, ApJ, 744, 112
Liszt H. S., Pety J., Lucas R., 2010, A&A, 518, A45
Loubser S. I., Sánchez-Blázquez P., Sansom A. E., Soechting I. K., 2009, MNRAS, 398, 133
McDonald M., Veilleux S., Rupke D. S. N., Mushotzky R., 2010, ApJ, 721, 1262
McDonald M., Veilleux S., Rupke D. S. N., Mushotzky R., Reynolds C., 2011, ApJ, 734, 95
McNamara B. R., Nulsen P. E. J., 2007, ARA&A, 45, 117
McNamara B. R., Nulsen P. E. J., 2012, New Journal of Physics, 14, 055023
McNamara B. R., O'Connell R. W., 1989, AJ, 98, 2018
McNamara B. R., O'Connell R. W., 1993, AJ, 105, 417
McNamara B. R., Jannuzi B. T., Sarazin C. L., Elston R., Wise M., 1999, ApJ, 518, 167
McNamara B. R. et al., 2000, ApJ, 534, L135
McNamara B. R. et al., 2001, ApJ, 562, L149 (M01)
McNamara B. R., Wise M. W., Murray S. S., 2004, ApJ, 601, 173
Magorrian J. et al., 1998, AJ, 115, 2285
Maiolino R., Caselli P., Nagao T., Walmsley M., De Breuck C., Meneghetti M., 2009, A&A, 500, L1
Mittal R., Hudson D. S., Reiprich T. H., Clarke T., 2009, A&A, 501, 835
Mittal R. et al., 2011, MNRAS, 418, 2386
Mittaz J. P. D. et al., 2001, A&A, 365, L93
Morris R. G., Fabian A. C., 2005, MNRAS, 358, 585
Morsony B. J., Heinz S., Brüggen M., Ruszkowski M., 2010, MNRAS, 407, 1277
Nulsen P. E. J., McNamara B. R., Wise M. W., David L. P., 2005, ApJ, 628, 629
O'Dea C. P., 1998, PASP, 110, 493
O'Dea C. P., Baum S. A., 1987, AJ, 94, 1476
O'Dea C. P., Baum S. A., 1997, in Soker N., ed., ASP Conf. Ser. Vol. 115, Galactic Cluster Cooling Flows. Astron. Soc. Pac., San Francisco, p. 147
O'Dea C. P., Baum S. A., Maloney P. R., Tacconi L. J., Sparks W. B., 1994a, ApJ, 422, 467
O'Dea C. P., Baum S. A., Gallimore J. F., 1994b, ApJ, 436, 669
O'Dea C. P., Payne H. E., Kocevski D., 1998, AJ, 116, 623
O'Dea C. P., Koekemoer A. M., Baum S. A., Sparks W. B., Martel A. R., Allen M. G., Macchetto F. D., Miley G. K., 2001, AJ, 121, 1915
O'Dea C. P., Baum S. A., Mack J., Koekemoer A. M., Laor A., 2004, ApJ, 612, 131
O'Dea C. P. et al., 2008, ApJ, 681, 1035
O'Dea K. P. et al., 2010, ApJ, 719, 1619
Oegerle W. R., Cowie L., Davidsen A., Hu E., Hutchings J., Murphy E., Sembach K., Woodgate B., 2001, ApJ, 560, 187
Oonk J. B. R., 2011, PhD thesis, Univ. Leiden
Oonk J. B. R., Jaffe W., Bremer M. N., van Weeren R. J., 2010, MNRAS, 405, 898
Oonk J. B. R., Hatch N. A., Jaffe W., Bremer M. N., van Weeren R. J., 2011, MNRAS, 414, 2309
Parma P., Murgia M., Morganti R., Capetti A., de Ruiter H. R., Fanti R., 1999, A&A, 344, 7
Parrish I. J., Quataert E., Sharma P., 2010, ApJ, 712, L194
Peres C. B., Fabian A. C., Edge A. C., Allen S. W., Johnstone R. M., White D. A., 1998, MNRAS, 298, 416
Peterson B. M., 1978, ApJ, 223, 740
Peterson J. R., Fabian A. C., 2006, Phys. Rep., 427, 1
Peterson J. R. et al., 2001, A&A, 365, L104
Peterson J. R., Kahn S. M., Paerels F. B. S., Kaastra J. S., Tamura T., Bleeker J. A. M., Ferrigno C., Jernigan J. G., 2003, ApJ, 590, 207
Pollack L. K., Taylor G. B., Allen S. W., 2005, MNRAS, 359, 1229
Quillen A. C. et al., 2008, ApJS, 176, 39
Rafferty D. A., McNamara B. R., Nulsen P. E. J., Wise M. W., 2006, ApJ, 652, 216
Rafferty D. A., McNamara B. R., Nulsen P. E. J., 2008, ApJ, 687, 899
Rawle T. D. et al., 2012, ApJ, 747, 29
Reynolds C. S., Heinz S., Begelman M. C., 2002, MNRAS, 332, 271
Robinson K. et al., 2004, ApJ, 601, 621
Romanishin W., 1987, ApJ, 323, L113
Rosner R., Tucker W. H., 1989, ApJ, 338, 761
Russell H. R. et al., 2012, MNRAS, 423, 236
Ruszkowski M., Begelman M. C., 2002, ApJ, 581, 223
Sakelliou I. et al., 2002, A&A, 391, 903
Salomé P., Combes F., 2003, A&A, 412, 657
Salomé P. et al., 2006, A&A, 454, 437
Salomé P., Combes F., Revaz Y., Downes D., Edge A. C., Fabian A. C., 2011, A&A, 531, A85
Sanders J. S., Fabian A. C., Allen S. W., Schmidt R. W., 2004, MNRAS, 349, 952
Sanders J. S., Fabian A. C., Allen S. W., Morris R. G., Graham J., Johnstone R. M., 2008, MNRAS, 385, 1186
Sarazin C. L., 1986, Rev. Mod. Phys., 58, 1
Sarazin C. L., McNamara B. R., 1997, ApJ, 480, 203
Sarazin C. L., Burns J. O., Roettiger K., McNamara B. R., 1995, ApJ, 447, 559
Shabala S. S., Ash S., Alexander P., Riley J. M., 2008, MNRAS, 388, 625
Sharma P., McCourt M., Quataert E., Parrish I. J., 2012, MNRAS, 420, 3174
Shostak G. S., Gilra D. P., Noordam J. E., Nieuwenhuijzen H., Vermue J., de Graauw T., 1980, A&A, 81, 223
Smith E. P., Heckman T. M., Illingworth G. D., 1990, ApJ, 356, 399
Smith E. P., Bohlin R. C., Bothun G. D., O'Connell R. W., Roberts M. S., Neff S. G., Smith A. M., Stecher T. P., 1997, ApJ, 478, 516
Soker N., Blanton E. L., Sarazin C. L., 2004, A&A, 422, 445
Solomon P. M., Downes D., Radford S. J. E., Barrett J. W., 1997, ApJ, 478, 144
Sparks W. B., Macchetto F., Golombek D., 1989, ApJ, 345, 153
Sparks W. B., Pringle J. E., Donahue M., Carswell R., Voit M., Cracraft M., Martin R. G., 2009, ApJ, 704, L20
Sparks W. B. et al., 2012, ApJ, 750, L5
Sun M., 2009, ApJ, 704, 1586
Sutherland R. S., Dopita M. A., 1993, ApJS, 88, 253
Tabatabaei F. S. et al., 2011, in print (arXiv:1111.6740)
Tamura T. et al., 2001, A&A, 365, L87
Taylor G. B., O'Dea C. P., Peck A. B., Koekemoer A. M., 1999, ApJ, 512, L27
Tozzi P., Norman C., 2001, ApJ, 546, 63
Tremblay G., 2011, PhD thesis, Rochester Institute of Technology
Tremblay G. R., O'Dea C. P., Baum S. A., Koekemoer A. M., Sparks W. B., de Bruyn G., Schoenmakers A. P., 2010, ApJ, 715, 172
Tremblay G. R. et al., 2012, MNRAS, in press (doi:10.1111/j.1365-2966.2012.21281.x)
Voigt L. M., Fabian A. C., 2004, MNRAS, 347, 1130
Voigt L. M., Schmidt R. W., Fabian A. C., Allen S. W., Johnstone R. M., 2002, MNRAS, 335, L7
Voit G. M., 1988, ApJ, 331, 343
Voit G. M., Donahue M., 1997, ApJ, 486, 242
Voit G. M., Donahue M., 2011, ApJ, 738, L24
Voit G. M., Cavagnolo K. W., Donahue M., Rafferty D. A., McNamara B. R., Nulsen P. E. J., 2008, ApJ, 681, L5
Wilman R. J., Edge A. C., Johnstone R. M., Fabian A. C., Allen S. W., Crawford C. S., 2002, MNRAS, 337, 63
Wilman R. J., Edge A. C., Swinbank A. M., 2009, MNRAS, 395, 1355
Wilman R. J., Edge A. C., McGregor P. J., McNamara B. R., 2011, MNRAS, 416, 2060
Wise M. W., McNamara B. R., Nulsen P. E. J., Houck J. C., David L. P., 2007, ApJ, 659, 1153
Wright A., Otrupcek R., 1990, PKS Catalog, 0
Xu H. et al., 2002, ApJ, 579, 600
ZuHone J. A., Markevitch M., Johnson R. E., 2010, ApJ, 717, 908

This paper has been typeset from a TEX/LATEX file prepared by the author.